

Key Points:

- Current feedback, as a physical process, slows down the Western Mediterranean Sea Circulation and reduces the intermittency of the currents
- It affects the mean barotropic vorticity budget and weakens the eddy-mean flow interaction
- It alters key features of the Western Mediterranean Sea Circulation, such as the Alboran Gyres and the Algerian Current

Correspondence to:

L. Renault,
lionel.renault@ird.fr

Citation:

Renault, L., Arsouze, T., & Ballabrera-Poy, J. (2021). On the influence of the current feedback to the atmosphere on the Western Mediterranean Sea dynamics. *Journal of Geophysical Research: Oceans*, 126, e2020JC016664. <https://doi.org/10.1029/2020JC016664>

Received 4 AUG 2020

Accepted 28 NOV 2020

On the Influence of the Current Feedback to the Atmosphere on the Western Mediterranean Sea Dynamics

L. Renault^{1,2} , T. Arsouze³ , and J. Ballabrera-Poy⁴ 

¹LEGOS, University of Toulouse, IRD, CNRS, CNES, Toulouse, UPS, France, ²University of California, Los Angeles, CA, USA, ³Barcelona Supercomputing Center (BSC), Barcelona, Spain, ⁴Institut de Ciències del Mar (CSIC), Barcelona, Spain

Abstract The ocean Current FeedBack to the atmosphere (CFB) has been shown to be an unambiguous physical process to achieve proper equilibrium in the Ocean. However, its effects on the Western Mediterranean Sea (WMS) are not known. In this study, eddy-rich coupled ocean-atmosphere simulations are carried out for the WMS to assess the extent to which CFB alters the WMS circulation and to characterize the low-level wind and surface stress responses to CFB. By generating conduits of energy from oceanic currents to the atmosphere, CFB slows the mean circulation by about 10% and acts as an oceanic eddy killer, reducing the mesoscale activity by 25% and attenuating the intensity of their intermittency. It also alters the mean barotropic vorticity balance of the WMS Gyre, reducing the role of wind stress curl, nonlinear torque, and bottom pressure torque. By reducing the eddy-mean flow interaction, CFB has a large influence on the properties of the Algerian Current, reducing the presence of standing eddies near Sardinia and improving the realism of the circulation. It also modifies the Alboran Gyres formation and the Northern Current retroflexion. Finally, coupling coefficients from the coupled simulations are estimated and are consistent with those for other regions. The CFB coupling coefficients can be used to parameterize the CFB in a forced ocean model. Overall, our results show that, as for other regions, the CFB is another physical mechanism to be considered for the representation of the WMS circulation.

Plain Language Summary The ocean Current FeedBack to the atmosphere (CFB) is the influence of the surface currents on the surface stress and wind. In the recent years, it has been shown to be a unambiguous physical process to achieve proper equilibrium in the Ocean. However its effects on the Western Mediterranean Sea (WMS) are not known. In this study, eddy-rich coupled ocean-atmosphere simulations are carried out for the WMS to assess the extent to which CFB alters the WMS circulation and to characterize the low-level wind and surface stress responses to CFB. We show that CFB induces conduits of energy from oceanic currents to the atmosphere, which in turn slow down the mean circulation by about 10% and damp the intermittency of the currents by 25%. CFB alters processes that controls the WMS circulation and largely modulates emblematic features of the WMS such as the Alboran Gyres and the Algerian Current. Finally, coupling coefficients are estimated and are consistent with those for other regions. The CFB coupling coefficients can be used to parameterize the CFB in a forced ocean model. Overall, our results show that the CFB is another physical mechanism to be considered for the representation of the WMS circulation.

1. Introduction

The Western Mediterranean Sea (WMS) is characterized by a roughly mean cyclonic circulation. Atlantic Waters (AW) enter in the surface layer through the strait of Gibraltar and flow along the North African Coast via the Alboran Gyres (e.g., Renault et al., 2012b; Vargas-Yáñez et al., 2002) and the Algerian Current to reach the Sicily channel (Millot, 1979). A significant contribution of the AW then flows to the Eastern part of the basin, while the other part reaches the northern rim of the basin in the Northern Current, and the Balearic Current via the Thyrenean Sea (e.g., Millot 1979). A relatively strong mesoscale activity affects the mean paths of circulation (e.g., Escudier et al., 2016). Algerian Current (Isern-Fontanet et al., 2003; Karimova, 2019; Puillat et al., 2002), Northern Current (Alberola et al., 1995; Guihou et al., 2013), Balearic

© 2020. The Authors.

This is an open access article under the terms of the [Creative Commons Attribution](https://creativecommons.org/licenses/by/4.0/) License, which permits use, distribution and reproduction in any medium, provided the original work is properly cited.

front (Bouffard et al., 2012; Mancho et al., 2008), or Thyrenean Sea (de la Vara et al., 2019) are typical places where mesoscale eddies lead to an important transport of heat, salt, and biogeochemical tracers over all the WMS. As shown by Escudier et al. (2016), unlike other regions of the World Ocean, eddies in the WMS do not have a preferred direction of propagation and appear to be mainly advected by mean currents. They are also characterized by a short life compared to other regions Isern-Fontanet et al. (2006). In the World Ocean, long-lived eddies are characterized by a lifetime of more than 16 weeks and by an average lifetime of 32 weeks (Chelton et al., 2011), whereas in the Mediterranean Sea, Isern-Fontanet et al. (2006) show that anticyclonic and cyclonic vortices have a mean lifetime of ≈ 2 months and 1 month, respectively. In the eastern Mediterranean Sea their life is considered to be longer than 8 weeks (Mkhinini et al., 2014), whereas in the WMS, long-lived eddies have a lifetime longer than 4 weeks, and only 1% of the eddies have a lifetime of more than 15 weeks (Escudier et al., 2016).

The WMS is also subject of intense air-sea-land interactions: the presence of several mountains ranges (e.g., Alps, Pyrenees) causes the existence of low-levels, cold air outbreaks associated with Tramotane, Cierzo, and Mistral winds (Jansá, 1987; Flamant, 2003), which induces strong sea surface temperature (SST) cooling and air-sea fluxes exchanges (Berthou et al., 2018; Estournel et al., 2003; Millot, 1979; Lebeaupin Brossier & Drobinski, 2009; Renault et al., 2012a; Ruiz et al., 2012). This strong air-sea coupling is of prime importance as this can lead to severe precipitations close to the coast (Berthou et al., 2016; Meroni et al., 2018) and even extreme oceanic events such as oceanic deep convection (Somot et al., 2018; Testor et al., 2018) that further affect water masses distribution and characteristics in all the basin.

In the past decades, the use of satellite observations and numerical coupled models have demonstrated the global ubiquity of mesoscale air-sea interactions and of their impacts on low-level wind and surface stress (Chelton & Xie, 2010; Chelton et al., 2001, 2007; Desbiolles et al., 2014; Gaube et al., 2015; Renault et al., 2016c, 2017a, 2019c). One of these processes, the thermal feedback (TFB), causes wind and surface stress magnitude, divergence, and curl anomalies (Chelton et al., 2004, 2007; O'Neill et al., 2010, 2012) in response to SST gradients (see Small et al., 2008 for a review). The TFB-induced stress curl anomalies generate Ekman pumping that modify the eddy propagation but not the eddy magnitude (Renault et al., 2020; Seo, 2017; Seo et al., 2016). Another of such processes is the Current FeedBack (CFB) that is the influence of the surface oceanic current on the surface stress and wind. It mainly affects the wind and stress curl. CFB has a bottom-up effect on the wind: a negative current anomaly creates a positive stress anomaly, which in turn induces a negative wind anomaly (Renault et al., 2016c, 2019c; Takatama & Schneider, 2017). At the larger scales, CFB causes a slow-down of the mean oceanic currents (e.g., Luo et al. 2005; Pacanowski 1987; Renault et al. 2016b). The (sub)mesoscale effect was less obvious and has been first suggested by Bye (1985) in a forerunner study but then has been largely ignored. Recently, the advent of eddy-rich coupled models has allowed to confirm it. The local effect of CFB consists of an eddy-killing mechanism, i.e., a damping by $\approx 30\%$ of the mesoscale and submesoscale activities (Dewar & Flierl, 1987; Oerder et al., 2018; Renault et al., 2016c, 2016b, 2017b, 2018, 2020; Seo, 2017; Seo et al., 2016). This effect is induced by the transfer of energy from oceanic currents to the atmosphere (Duhaut & Straub, 2006; Renault et al., 2016c, 2017a; Scott & Xu, 2009; Xu & Scott, 2008). CFB, through the *eddy killing* mechanism, opens a tight control on Western boundary currents by reducing the eddy-mean flow interaction (Renault et al., 2019b). By providing an undeniable energy sink mechanism, CFB happens to correct some long-standing modeling biases in the representation of oceanic mesoscale activity, Western Boundary Currents and eddy-mean flow interaction.

The CFB effect on the WMS circulation has not been assessed yet, nor has a proper characterization of the mesoscale low-level wind and surface stress response to both CFB and TFB. In this study, the main goal is to assess to which extent CFB can partly drive the WMS oceanic circulation at both large scale and mesoscale. As a secondary objective, this study attempts to characterize the low-level wind and surface stress responses to the mesoscale CFB and TFB. To respond to these objectives, a set of two realistic mesoscale resolving ocean and atmosphere coupled simulations, implemented over the WMS for a period of 7 years, is carried out. The study is organized as follows: Section 2 describes the model configuration and the main methodology. In Section 3, the alteration of the mean WMS circulation is addressed. Section 4 is devoted to determine the extent to which CFB modulates the mesoscale activity and the surface currents intermittency. In Section 5, a focus on emblematic features of the WMS allows to better understand how CFB can alter them. Finally, Section 6 aims to characterize the low-level wind and surface stress responses to both CFB and TFB. The results are discussed in Section 7, which is followed by the conclusion.

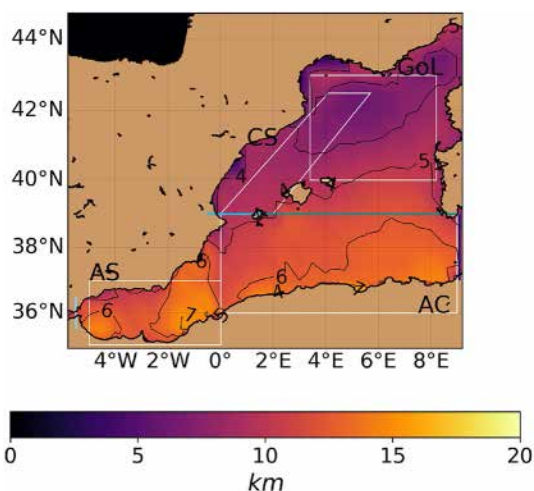


Figure 1. The Western Mediterranean Sea. The color field represents the first Rossby radius of deformation as estimated from CARS (Ridgway et al., 2002) following Chelton et al. (1998). The black contours show the ratio between the Rossby radius of deformation and the spatial resolution of the oceanic model. The white boxes highlight the regions used in the hereafter analysis: the Alboran Sea (AS), the Algerian Current (AC), the Gulf of Lions (GoL), and the Catalan Sea (CS). The four blue lines highlight the sections used in the particle analysis 5.3.

2. Model Configuration and Methodology

2.1. The Coastal and Regional Ocean Community Model

The oceanic simulations were performed with the coastal and regional ocean community (CROCO) model (Debreu et al., 2012), developed around the kernel of the regional oceanic modeling system (ROMS) (Shchepetkin, 2015; Shchepetkin & McWilliams, 2005, 2009). CROCO is a free-surface, terrain-following coordinate model with split-explicit time stepping and with Boussinesq and hydrostatic approximations. As in Sayol et al. (2013) and Juza et al. (2016), CROCO is implemented over the WMS from the Alboran strait to the Corsica and Sardinia straits (Figure 1, from 5.8°W to 9.2°E and 34.9°N to 44.7°N) with a resolution of ≈ 2 km. Such a spatial resolution allows to fully resolve the oceanic mesoscale activity almost everywhere in the Western Mediterranean Sea, except in some shallow places near the Gulf of Lions (Figure 1). Temperature, salinity, surface elevation, and horizontal velocity initial and boundary information are taken from the Mediterranean forecasting system (MFS, Tonani et al., 2011) daily reanalysis. The configuration has 50 levels in the vertical with the same vertical grid system concentrating vertical levels near the surface (Shchepetkin & McWilliams, 2009), with stretching surface and bottom parameters $h_{\text{cline}} = 300$ m, $\theta_b = 2$, and $\theta_s = 7$. Bathymetry is constructed from the shuttle radar topography mission (SRTM30 plus) data set (available at http://topex.ucsd.eduWWW_htmlsrtm30_plus.html) based on the 1-min Sandwell and Smith (1997) global data set and higher-resolution data where available. To avoid aliasing and to ensure

the smoothness of the topography at the grid scale, a Gaussian smoothing kernel with a width of four times the topographic grid spacing is used. Additionally, to ensure a weak pressure gradient errors induced by terrain-following (σ), a local smoothing of the topography is applied where the steepness of the topography exceeds a factor $r = 0.2$. Finally, vertical mixing of tracers and momentum is done with a K-profile parameterization (KPP; Large et al., 1994). Monthly climatological freshwater discharges of the Rhone and the Ebro rivers (Dai & Trenberth, 2002) are included in the model as point sources.

2.2. The Weather Research and Forecast Model

Weather research and forecast (WRF; version 3.7.1, Skamarock et al., 2008) is implemented over a similar domain except that it covers the Alps and has at least five more points in all the directions (corresponding to the WRF sponge). It has a spatial resolution of ≈ 7 km, which is enough to resolve the mesoscale air-sea interactions represented by the ≈ 2 km ocean grid (Jullien et al., 2020). The simulation is initialized and forced at the open boundary condition with the climate forecast system reanalysis (CFSR) (≈ 40 km spatial resolution; Saha et al., 2010). Forty vertical levels are used, with half of them in the lowest 1.5 km. The parameterizations used here are similar to the one employed in Renault et al. (2016b), and the reader is invited to refer to that study for more details. A bulk formula is used (Fairall et al., 2003) to estimate the freshwater, turbulent, and momentum fluxes provided to CROCO. Note that because of the implicit treatment of the bottom boundary condition in most atmospheric models, the use of CFB involves a modification of both the surface-layer vertical mixing Lemarié (2015) parameterization (MYNN2.5 in our case, Nakanishi & Niino 2006) and the tridiagonal matrix for vertical turbulent diffusion. Ignoring these modifications causes a large underestimation of the CFB effects on the wind and surface stress and on the associated oceanic response (Renault et al., 2019a).

2.3. Experiments

The data are exchanged between CROCO and WRF every hour using the OASIS3-MCT coupler (Valcke, 2013). A coupling frequency of 1 h allow to resolve correctly the diurnal cycle, the synoptic variations

of the wind as well as the inertial currents. Note that a coupling frequency of less than 1 h would require coupling with a wave model. In the first experiment, named NOCRT, WRF gives CROCO the hourly averages of heat, momentum, and freshwater fluxes; whereas, CROCO gives to WRF the hourly averaged SST. The surface stress is estimated using the absolute wind U_a , i.e., ignoring CFB. The second experiment, named CRT, is the very same experiment except that CROCO sends to WRF both SST and the surface current U_o . In CRT, the surface stress is estimated using the relative wind to the oceanic motions:

$$U = U_a - U_o \quad (1)$$

Both experiments start from the same initial conditions from January 1, 2002 and are integrated for 7 years. The two first years are discarded as a spin-up.

2.4. Eddy Kinetic Energy and Energy Conversion

CROCO-WMS configuration is eddy-resolving in most of the domain (Figure 1). In order to study the influence of the eddy-killing effect of the CFB on the circulation, we define some standard metrics to perform a simplified energy budget analysis over the domain.

In the following, the overbar ($\overline{}$) stands for seasonal means (estimated over the 2004–2008 period), whereas the deviations from the seasonal means are referred by using primes ($'$). The eddy kinetic energy (EKE) is estimated using the surface currents or the geostrophic currents as:

$$EKE = \sqrt{U_o'^2 + V_o'^2} \quad (2)$$

with U_o and V_o the surface total or geostrophic (U_{og} and V_{og}) zonal and meridional currents, respectively. As detailed in Renault et al. (2016c), the mean geostrophic wind work and the eddy wind work are estimated in the following:

$$F_m K_m = \frac{1}{\rho_0} (\overline{U_{og} \tau_u} + \overline{V_{og} \tau_v}) \quad (3)$$

and

$$F_e K_e = \frac{1}{\rho_0} (\overline{U_{og}' \tau_u'} + \overline{V_{og}' \tau_v'}) \quad (4)$$

where ρ_0 is the mean seawater density (taken as $1,025 \text{ kg m}^{-3}$), τ_u and τ_v are the zonal and meridional surface stresses. $F_m K_m$ represents the transfer of energy from the atmosphere to mean kinetic energy and $F_e K_e$ represents the exchange of energy from low-level wind anomalies to the mesoscale activity. As in Marchesiello et al. (2003), we also focus on the following relevant energy source terms, which are the baroclinic and barotropic instabilities:

$$P_e K_e = \int_z -\frac{g}{\rho_0} \overline{\rho' w'}, \quad (5)$$

$$K_m K_e = \int_z -(\overline{u_o' u_o'} \frac{\partial u_o}{\partial x} + \overline{u_o' v_o'} \frac{\partial u_o}{\partial y} + \overline{u_o' w'} \frac{\partial u_o}{\partial z} + \overline{v_o' u_o'} \frac{\partial v_o}{\partial x} + \overline{v_o' v_o'} \frac{\partial v_o}{\partial y} + \overline{v_o' w'} \frac{\partial v_o}{\partial z}), \quad (6)$$

where g is the gravitational acceleration, w is the vertical velocity in the ocean, and x , y , and z are the zonal, meridional, and vertical coordinates, respectively.

2.5. Barotropic Vorticity Budget

The Oceanic gyre circulation can be understood as the mean of the barotropic vorticity budget, which is a generalization of Sverdrup balance. Following e.g., Schoonover et al. (2016), the barotropic vorticity budget is estimated by computing the rotational of the vertically integrated lateral momentum equations:

$$\frac{\partial \bar{\zeta}}{\partial t} = \frac{J(P_b, h)}{\rho_0} - \mathcal{A} - \nabla \cdot (f\mathbf{U}) + \frac{\nabla \times \boldsymbol{\tau}}{\rho_0} - \frac{\nabla \times \boldsymbol{\tau}_b}{\rho_0} + \mathcal{D} \quad (7)$$

where $\partial \bar{\zeta} = (\nabla \times (\mathbf{U})) \cdot \hat{z}$ is the barotropic vorticity; \mathbf{U} is the barotropic current; J is the Jacobian operator, P_b is the bottom pressure; h is the bathymetry; \mathcal{A} is the non-linear torque; f is the Coriolis force; $\boldsymbol{\tau}_b$ is the bottom stress; and \mathcal{D} is the viscous torque (including the torque introduced by subgrid-scale parameterizations). In the following, the terms of the right-hand side of Equation 7 are referred to the bottom pressure torque $\left(\frac{J(P_b, h)}{\rho_0}\right)$, the nonlinear torque $(-\mathcal{A})$, the planetary vorticity advection $(-\nabla \cdot (f\mathbf{U}))$, the surface stress curl $\left(\frac{\nabla \times \boldsymbol{\tau}}{\rho_0}\right)$, the bottom stress curl $\left(-\frac{\nabla \times \boldsymbol{\tau}_b}{\rho_0}\right)$, and the viscous torque (\mathcal{D}) .

The bottom pressure torque is the twisting force that results from the variation of the bottom pressure P_b along the isobaths. The bottom pressure torque is a measure of the topographic steering of the flow and does not drive by itself the flow. It does not represent any dissipation nor energy input and is determined dynamically by the ocean flow (see also Jackson et al., 2006 for a detailed description of the bottom pressure torque). The nonlinear torque represents the advection of vorticity by the mean flow and by the eddies. The planetary vorticity advection arises from the Coriolis effect. The surface stress curl can be considered as a top drag. It is externally imposed by the atmosphere and can lead to an input or a dissipation of energy. The bottom stress curl is the drag that is imposed by the topography. Finally, the viscous torque represents the model diffusion. In a regional numerical simulation, it can have large values over the sponges.

2.6. Coupling Coefficients

As in Renault et al. (2016c, 2019c), we define the following two coupling coefficients related to the CFB:

- s_r is defined as the slope of the linear regression of the mesoscale surface current vorticity and the mesoscale surface stress curl
- s_w is defined as the slope of the linear regression of the mesoscale surface current vorticity and the mesoscale 10-m wind curl

Chelton et al. (2007) (among many other studies in the literature) define four TFB coupling coefficients:

- sC_{str} and sC_w are defined as the slopes of the linear regression of the mesoscale stress/wind curl and cross-stress/wind SST gradient
- sD_{str} and sD_w are defined as the slopes of the linear regression of the mesoscale stress/wind divergence and down-stress/wind SST gradient

In all these coefficients, the mesoscale anomalies are isolated using a Gaussian spatial high-pass filter (cut-off of 50 km) and a 29-days running window. Note that a larger filter (e.g., 250 km) does not significantly change the results. Renault et al. (2019c) provide the full method how to estimate these coupling coefficients.

3. Mean Circulation

As a first evaluation of the mean WMS circulation, the mean sea surface height (SSH) and the barotropic stream function $\Psi(x, y)$ are estimated from the 5 years of NOCRT. Here Ψ is computed by integrating the meridional transport eastward and imposing $\Psi = 0$ on the coastline of the Gulf of Lions. The mean SSH is also estimated from the observations from the $\frac{1}{8}^\circ$ resolution Archiving, Validation and Interpretation of

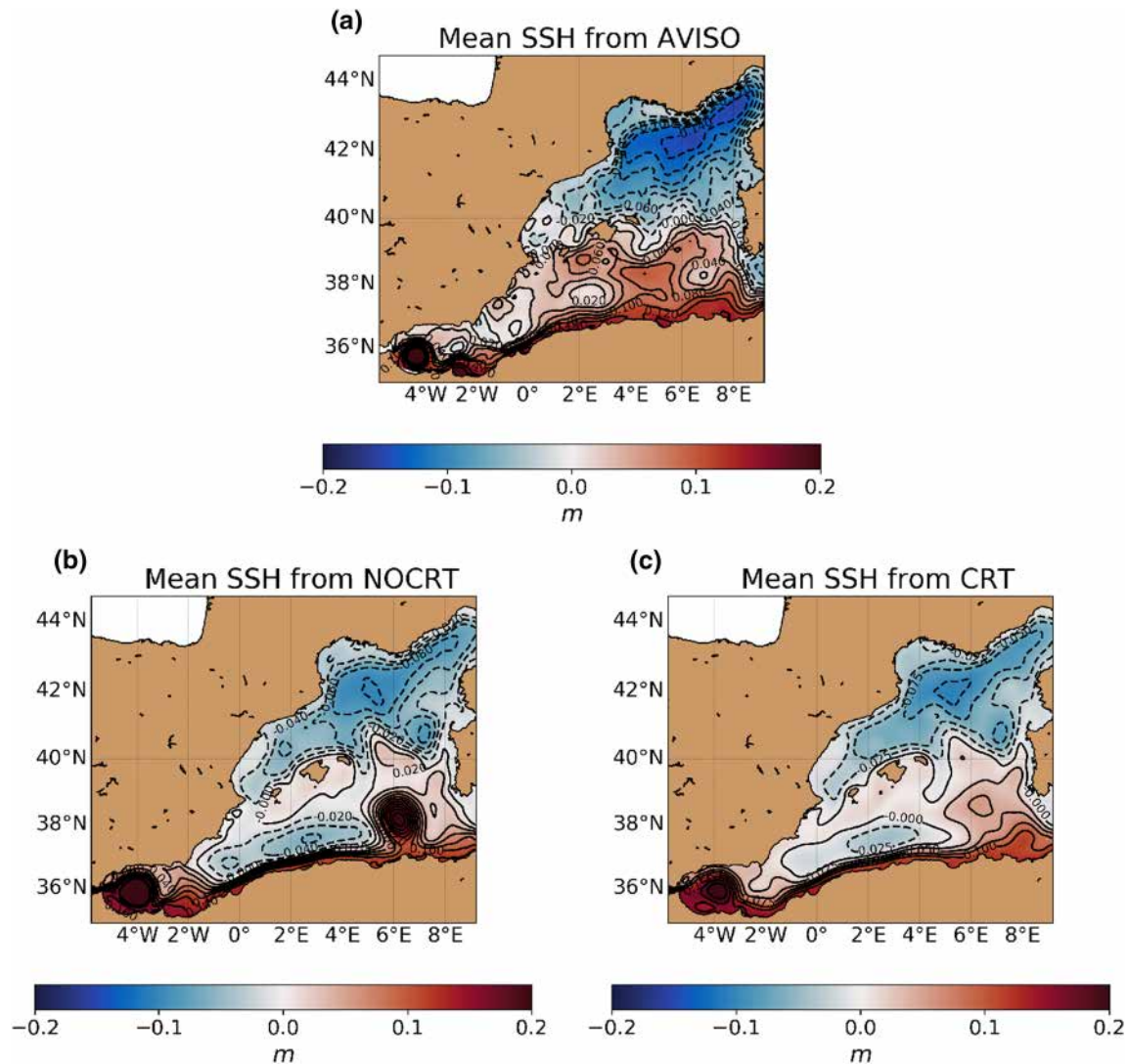


Figure 2. Mean sea surface height (SSH) from (a) the AVISO product, (b) the simulation without CFB (NOCRT), and (c) the simulation with CFB (CRT). CFB, current feedBack to the atmosphere. AVISO, Archiving, Validation and Interpretation of Satellite Oceanographic data.

Satellite Oceanographic (AVISO) data set over the same period (Rio et al., 2014) (Figures 2 and 3). In good agreement with the observations, NOCRT represents the main spatial patterns of the mean SSH and of the mean surface circulation such as the WMS cyclonic circulation, the Alboran gyres, the North Balearic Front and the Algerian Current (similar results are found using the mean geostrophic currents). The Algerian Current is characterized by a mean net transport by 9 Sv ($1 \text{ Sv} = 10^6 \text{ m}^3 \text{ s}^{-1}$) and the Northern Current has the imprint of two kinds of retroflexions: the classic one in the Catalan Sea, and an upstream one in the Gulf of Lions, which is likely caused by the presence of eddies.

Despite its relative degree of realism and consistency with previous numerical studies (e.g., Beranger et al. 2010; Hamon et al. 2016; Sannino et al. 2015), NOCRT suffers from long-standing biases in the representation of the WMS mean circulation such as e.g., the persistence of an anticyclonic eddy near Sardinia and too weak currents along the northern rim of the WMS (Northern Current along the French and Spanish coast) and too strong currents along the Southern rim of the WMS (Alboran Gyres, Algerian Current). From NOCRT to CRT, CFB slows down both the mean net barotropic transport (Figure 3) and the mean surface currents (not shown) by about 10%. This is likely partly explained by the reduction of the surface stress and $F_m K_m$ by $\approx 15\%$ induced by CFB (not shown), which is consistent with Pacanowski (1987), Luo et al. (2005),

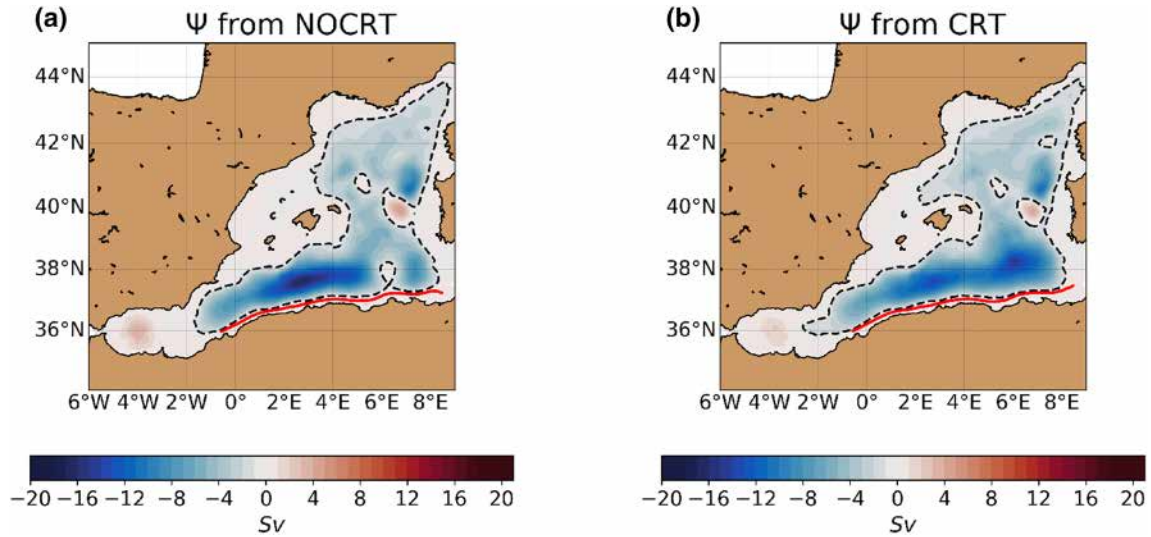


Figure 3. Mean stream function from the simulation (a) without CFB (NOCRT), and (b) the simulation with CFB (CRT). CFB leads to a reduction of the mean barotropic transport. The red line highlights the Algerian Current (highlighted using the 0 Sv contour) whereas the dashed black contour shows the WMS Gyre defined by using the Ψ contour of -1 Sv. Three main regions are impacted by CFB: the Alboran Sea, the Algerian Current, and the Northern current retroflexion region (Gulf of Lions/Catalan Sea). CFB, current feedBack to the atmosphere.

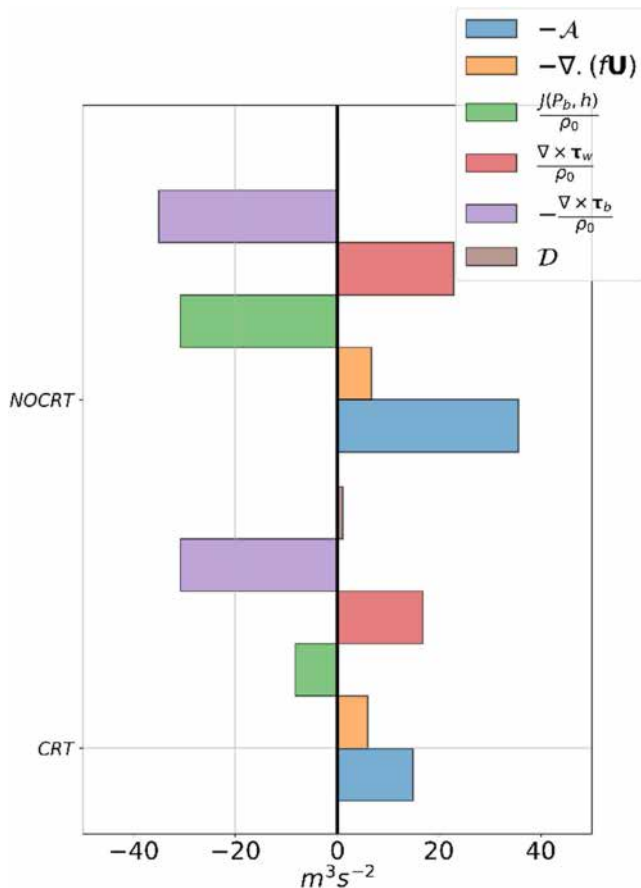


Figure 4. Time-average of the integrated barotropic vorticity budget for the Western Mediterranean Gyre highlighted in Figure 3.

and Renault et al. (2016b) for other regions. In NOCRT, the presence of standing eddies that detach from the Algerian Current near Sardinia causes a large northward deflection of the mean current, which is unrealistic. CFB reduces this behavior, improving the realism of the simulation. Sections 4.1 and 5 aim to better understand what mechanisms are involved. The retroflexion of the North Current is also altered by CFB.

To better understand what drive the WMS gyre circulation and the extent to which CFB can alter it, following e.g., Schoonover et al. (2016) and Le Corre et al. (2020), the long-term averaged barotropic vorticity budget is estimated over the WMS Gyre (Figure 4) by using a closed barotropic stream function contour of -1 Sv (highlighted in Figure 3). In both NOCRT and CRT, the WMS gyre is not in a Sverdrup balance as the balance is not achieved between the surface stress curl $\left(\frac{\nabla \times \tau}{\rho_0}\right)$ and the planetary vorticity advection $(-\nabla \cdot (fU))$.

In the WMS, cyclonic vorticity generation arises from surface stress curl $\left(\frac{\nabla \times \tau}{\rho_0}\right)$ but also from nonlinear torque (A) , which likely advects cyclonic vorticity from the coastal regions and the Alboran Sea. In NOCRT, the balance is achieved by both the bottom drag $\left(-\frac{\nabla \times \tau_b}{\rho_0}\right)$ and the bottom pressure torque $\left(\frac{J(P_b, h)}{\rho_0}\right)$, indicating large

variation of the bottom pressure P_b along the isobath. In CRT, CFB appears to have a significant control on the barotropic vorticity budget. On the one hand, it reduces the generation of positive vorticity by wind stress curl $\left(\frac{\nabla \times \tau}{\rho_0}\right)$, which is consistent with the reduction of the surface stress. On the other hand, CFB also reduces the effect of the non-linear torque

$(-A)$, which traduces the slow-down and of the mean circulation by CFB but also, as demonstrated in Section 4.1, the damping of the mesoscale activity. Unlike NOCRT, at the first order, in CRT, the balance is only achieved by bottom drag $\left(-\frac{\nabla \times \tau_b}{\rho_0}\right)$, which is barely affected by CFB. CFB largely mitigates the bottom pressure torque effect that becomes very weak from NOCRT to CRT. The large reduction of bottom pressure torque can also be interpreted as a reduction of the P_b variations along the isobath and, thus, as a flattening of the isopycnals. In the WMS, a simulation that neglects CFB may overestimate the nonlinear torque and the surface stress curl but also the role of bottom pressure torque in determining the WMS circulation.

To conclude this section, Figures 2 and 3 reveal three main regions that are the most impacted by CFB and that are therefore the focus of the following sections: the Alboran Sea, the Algerian Current, and the Northern Current.

4. Mesoscale Activity

4.1. Damping of the Mesoscale Activity

As a measure of the oceanic mesoscale activity, Figures 5a–5c shows the surface EKE estimated using daily surface currents from drifters trajectories (Poulain et al., 2012) and from NOCRT. As in Escudier et al. (2016), velocities of drifters are edited to remove outliers, interpolated, filtered at 36 h to remove high-frequency oscillations and subsampled. The measured current does not only represent the geostrophic currents but also Ekman currents that are not removed. The EKE is estimated from this product by binning the velocities within boxes of 0.5° .

Consistent with the literature, simulations and drifters reveal the presence of large levels of EKE over the Alboran Sea, the Algerian Current, and to a less extent the Gulf of Lions and the Catalan Sea, i.e., regions where the mean currents are relatively strong and can feed the mesoscale activity (see Section 4.3). In NOCRT, the spatial-mean EKE over the whole domain is overestimated by 20% (from $\approx 240 \text{ cm}^2 \text{ s}^{-2}$ to $300 \text{ cm}^2 \text{ s}^{-2}$) with respect to the drifters estimate. The overestimation is even larger than 50% over the Alboran Sea, and over the Algerian Current near Sardinia where standing eddies are too intense and likely too frequent. As demonstrated in Section 5, this excess of EKE near Sardinia induces a too strong eddy mean flow interaction, explaining the imprint of these eddies on the mean surface current (Figure 2). Noteworthy, along the Algerian Current, between 0°E and 5°E , the EKE in NOCRT is excessively attached to the coast and does not spread offshore with respect to the drifters, likely because the Algerian Current in NOCRT is too stable over that portion. This could be due to a too smooth topography or coastline.

The EKE is also often computed from satellite geostrophic currents and from the simulated surface geostrophic currents (Figure 5b). However, due to the interpolation procedure and to the satellites repetitivity, AVISO currents are only able to resolve eddies longer than a week (Chelton et al., 2001). Amores et al. (2018) demonstrate that the EKE estimated from AVISO is likely to be underestimated by a factor between two and three in the Mediterranean Sea, which is also in agreement with the drifters estimate in Figure 5. Note that the ageostrophic portion of EKE can be estimated from NOCRT and represents less than 10% of the total EKE. Due to this high level of underestimation and uncertainty of EKE estimations by satellite products, we decided to not use this AVISO data set.

The surface EKE is furthermore estimated from CRT using the total surface current and is compared to NOCRT and to the drifters in Figure 5. The EKE in CRT has a realistic spatial distribution and level of energy with respect to drifters observations. Overall the domain, the spatial-mean of the EKE is $225 \text{ cm}^2 \text{ s}^{-2}$, which is in agreement with the drifters estimate ($240 \text{ cm}^2 \text{ s}^{-2}$). Consistent with the literature for other regions, the CFB acts as an eddy killer: from NOCRT to CRT, the domain-averaged EKE is damped by $\approx 25\%$ (Figure 5). Some biases are still present such as the too-low level of EKE between 0°E and 5°E . In CRT, the Gulf of Lions and the Catalan may have a slightly too low an EKE, which could be due to the fact that the model is not fully mesoscale resolving in that region (see Rossby Radius in Figure 1). The main drivers of the EKE damping are assessed in the next section.

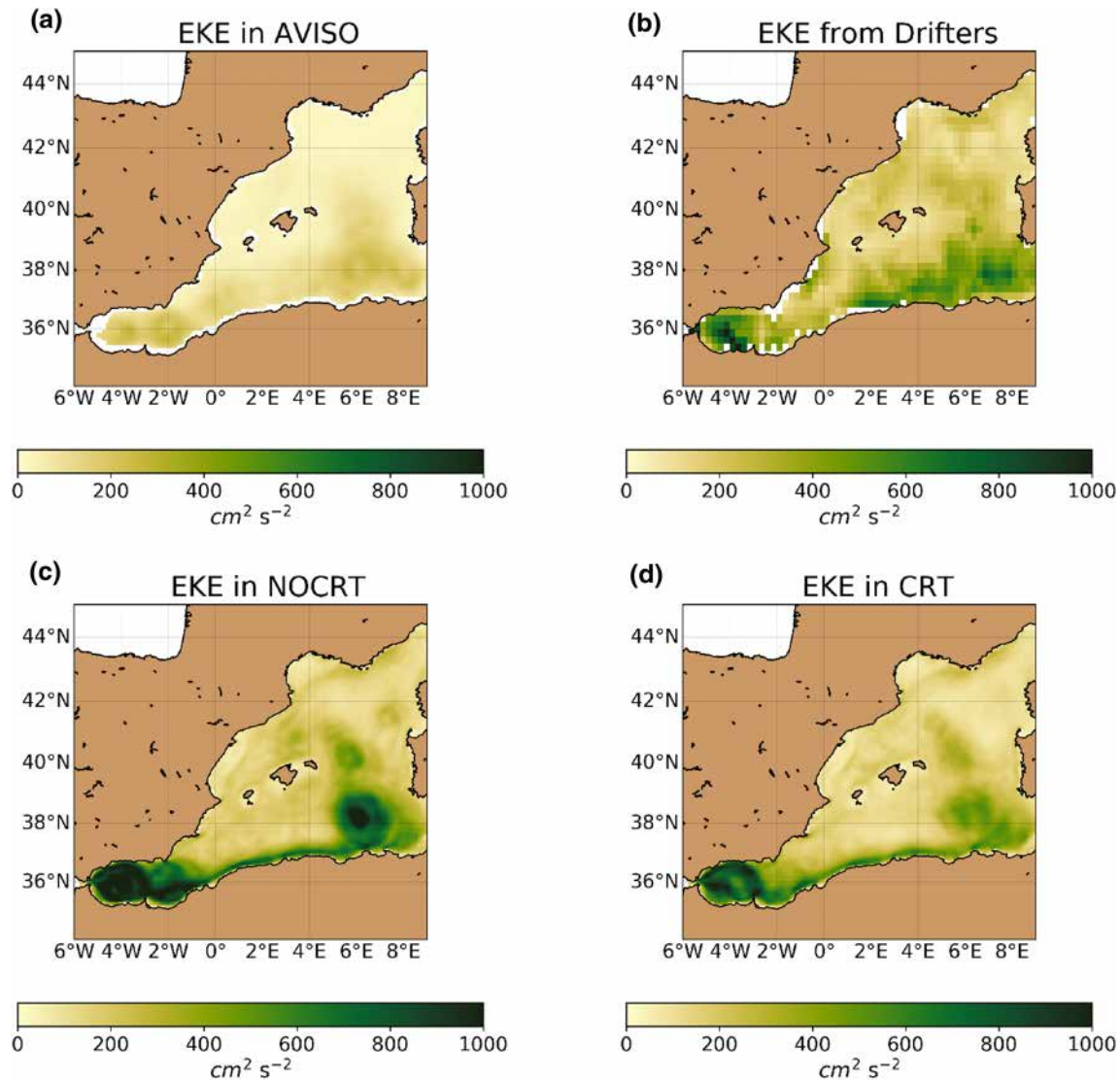


Figure 5. Mean surface Eddy kinetic energy from (a) drifters (see Section 4.1), (b) geostrophic currents from AVISO, (c) the simulation without CFB (NOCRT), and (d) the simulation with CFB (CRT). From NOCRT to CRT, CFB induces a large damping of the mesoscale activity (by $\approx 25\%$), improving the EKE realism with respect to drifters observations. In particular, CFB reduces the intensity of standing eddies near Sardinia. AVISO largely underestimates the EKE. CFB, current feedBack to the atmosphere. AVISO, Archiving, Validation and Interpretation of Satellite Oceanographic data.

4.2. Reduction of the Intermittency of Surface Currents

The damping of the mesoscale activity and the slow-down of the mean currents can be furthermore confirmed by comparing the Probability Density Function (PDF) of the surface current velocity from the drifters, NOCRT, and CRT (Figure 6). Reproduce in a model the PDF of surface current velocities is crucial for dispersion studies based on numerical modeling. To be comparable to the drifters estimates, the surface currents from the simulations are smoothed over two days. Mean, Median, and Standard Deviation of the surface current velocities are also shown in Table 1. The PDF from NOCRT is clearly shifted toward the largest values, indicating that NOCRT overestimates the velocity of the mean (and the median, see also Table 1) currents with respect to the drifters observations. Velocities larger than 25 cm s^{-1} are too often present in NOCRT, confirming a too large variability in NOCRT (see also Table 1). This can be explained by the lack of CFB. Indeed, the PDF estimated from CRT is much closer to the observations. CFB by slowing down the mean currents and by damping the mesoscale activity reduces the surface current velocities and their variability (see also Table 1).

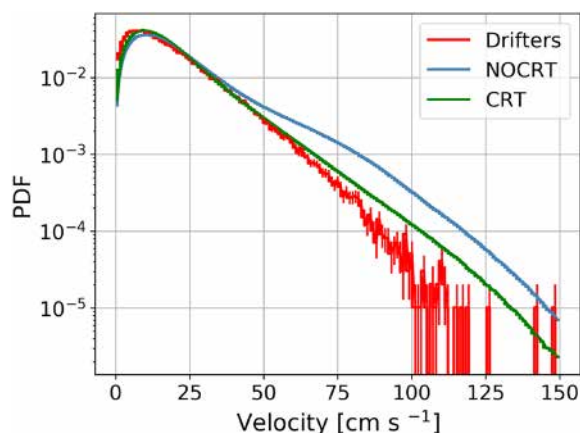


Figure 6. Probability density function of surface current velocity from drifters (red), NOCRT (blue), and CRT (green). The surface currents from the simulations have been smoothed using a two-day window to be comparable to drifters estimate. The error bar is estimated as the square root of the count of each bin. The number of bins (150) is estimated based on Freedman and Diaconis (1981).

4.3. Energy Conversion and Sink of Energy

To diagnose which processes drive the mesoscale activity reduction, following Marchesiello et al. (2003), a simplified EKE budget is computed from NOCRT and CRT (see Section 2 and Figure 7) and is averaged over the Alboran Sea, the Algerian Current, and the Catalan Sea (See boxes shown in Figure 1).

Over the Algerian Current, both $K_m K_e$ and $P_e K_e$ are important in explaining the generation of eddies. CFB, by reducing the mean eddy wind work ($F_m K_m$) by $\approx 15\%$ (not shown), causes a slow-down of the mean currents and a weakening (increase) of the barotropicity (baroclinicity) of the Algerian Current. As a result, it diminishes $K_m K_e$ by $\approx 40\%$ but doubles $P_e K_e$. The net conversion of energy from baroclinic and barotropic instabilities remains finally the same from NOCRT to CRT. In the Alboran Sea, $K_m K_e$ and $P_e K_e$ are both significant while over the Catalan Sea, $K_m K_e$ is second-order mechanisms (similar result is found for the Gulf of Lions). However, in both regions, the energy conversion by $K_m K_e$ and $P_e K_e$ is barely affected by CFB, likely because, as for the Californian Upwelling (Renault et al., 2016c), the mean dynamics of these region is less strong than that of the Algerian Current (or Western Boundary Currents more generally).

Consistent with previous studies (Oerder et al., 2018; Renault et al., 2016c, 2016b, 2017b; Seo et al., 2016), the main effect of CFB consists to reduce $F_e K_e$ (by $\approx 50\%$) by transferring energy from mesoscale currents toward the atmosphere. Note that here $F_e K_e$ is positive because it is estimated using a Reynolds decomposition that is based on a temporal filter. Such a filter does not capture only the atmospheric response to the CFB but all kind of “eddy wind work” (e.g., alongshore wind-driven currents). The sink of energy induced by the CFB can be furthermore estimated by considering the stress and current anomalies using a high-pass Gaussian spatial filter with a 50 km cut-off (Figure 8a). In such an estimate, $F_e K_e$ is negative almost everywhere, revealing the transfer of energy from mesoscale currents to the atmosphere. The few positive values corresponds to remaining wind-driven currents or e.g., to wind expansion fans effects (Winant et al., 1988). Note that AVISO and QuikSCAT cannot be used to estimate a realistic $F_e K_e$ because of limitations mainly due to their effective spatial resolution (Renault et al., 2017a), even in this region. In CRT, the still too low EKE between 0°E and 5°E over the Algerian Current is likely due to a weak generation of eddies by barotropic instability.

Finally, a spatial co-spectrum analysis of the geostrophic wind work (similar results are found with the total wind work) is performed using the daily surface stress and geostrophic currents for the Algerian Current and the Gulf of Lions (Figure 8b and see boxes on Figure 1). In CRT, the sinks of energy induced by CFB are clearly revealed by large negative values of the wind work co-spectrum from wavelength of 15 km to more than 200 km that are not present in NOCRT. Note that at the large scale, the wind work should be positive but the boxes used here are too small to significantly reflect it.

5. Dynamical Features Affected by CFB

In this section, we focus on some of the most remarkable dynamics of the WMS, and how they are affected by CFB.

5.1. Eddy Mean Flow Interactions

In the ocean, eddies feedback energy to the large-scale circulation through eddy-mean flow interaction (the inverse cascade of energy, Capet et al., 2008; LaCasce, 2012). An excessive mesoscale activity can induce a too large an eddy-flow interaction and destabilizes the mean

Table 1
Statistics of Surface Current Velocity from Drifters and the Simulations

	Mean (cm s ⁻¹)	Median (cm s ⁻¹)	Standard deviation (cm s ⁻¹)
Drifters	18.0	14.4	14.2
NOCRT	22.9	17.7	18.6
CRT	19.5	15.6	15.1

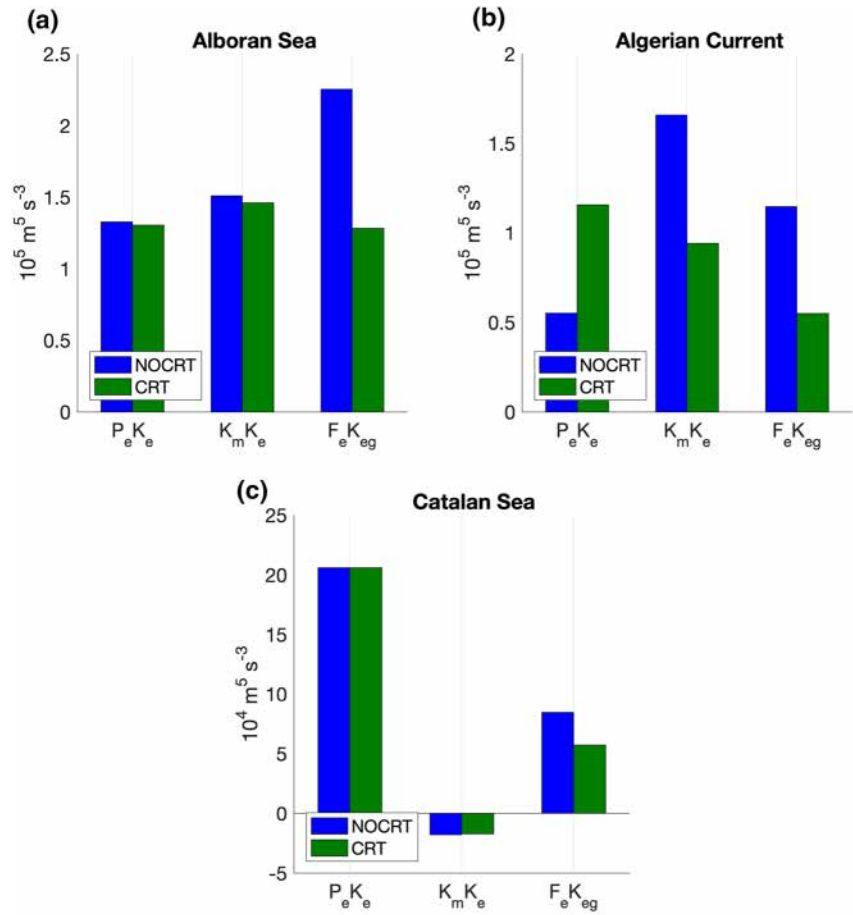


Figure 7. Depth-integrated simplified EKE-budget components based on a temporal Reynolds decomposition ($\text{m}^5 \text{s}^{-3}$) from NOCRT (blue) and CRT (green) over (a) the Alboran Sea, (b) the Algerian Current, and (c) the Catalan Sea. The eddy wind work ($F_e K_{eg}$) is positive due to the presence of wind-driven currents along the coast.

currents (Renault et al., 2019b), like e.g., the formation of the Alboran Gyres in the WMS. As in Marchesiello et al. (2011), Arbic et al. (2013), and Renault et al. (2019b), the spectral kinetic energy flux $\Pi(k)$, i.e., the energy transfer rate in k space, is estimated from NOCRT and CRT. $\Pi(k)$ is computed as the integral in k of the KE advection term $A(k)$ (assuming that the flux vanishes at the highest wavenumber k_{max}):

$$A(k) = A_H(k) + A_V(k) = \Re \left[-\widehat{\mathbf{u}_h^*} \cdot \widehat{(\mathbf{u}_h \cdot \nabla) \mathbf{u}_h} - \widehat{\mathbf{u}_h^*} \cdot w \frac{\partial \widehat{\mathbf{u}_h}}{\partial z} \right] \quad (8)$$

where the caret denotes a horizontal Fourier transform after removing the areal mean and performing symmetrization, to avoid edge effects in the periodization process. The asterisk notation $*$ indicates the complex conjugate operator; the symbol \Re represents the real-part operator; the overbar represents an average in time over the whole period of the simulation (5 years). $\Pi(k)$ is furthermore estimated as:

$$\Pi(k) = \int_k^{k_{max}} A dk \quad (9)$$

As in Renault et al. (2019b), the error associated to $\Pi(k)$ is assessed using a bootstrap method. $\Pi(k)$ is then estimated over the Alboran Sea, the Algerian Current, the Catalan Sea, and the Gulf of Lions (Figure 9). Renault et al. (2019b) demonstrate that CFB leads to more realistic representation of Western Boundary Current through *eddy killing* that mitigates the interaction between eddies and the mean flow. Such a reduction

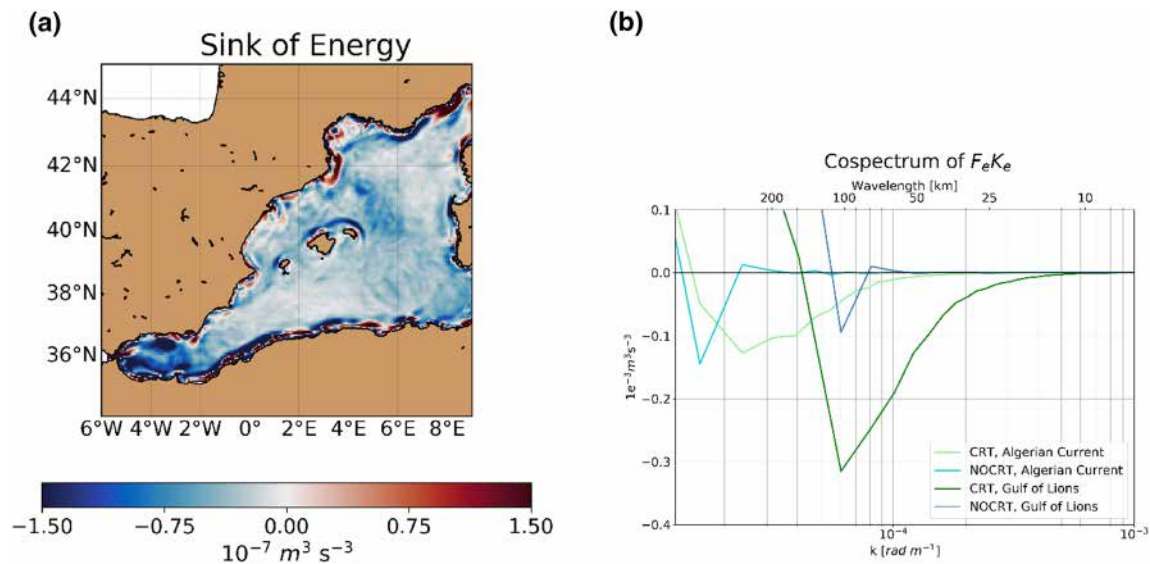


Figure 8. Exchange of energy between oceanic mesoscale currents and the atmosphere. (a) Spatial distribution of the eddy wind work estimated from CRT using a spatial filter, allowing to filter out most of the wind-driven currents. (b) Co-spectrum of $F_e K_e$ over the Algerian Current and the Gulf of Lions (see boxes on Figure 1) from NOCRT (blue) and CRT (green). CFB causes sinks of energy from oceanic mesoscale currents to the atmosphere. CFB, current feedBack to the atmosphere.

is induced by the unambiguous physical energy sink mechanism. A similar result is found for the WMS where CFB reduces the inverse cascade of energy at the Alboran Sea, the Algerian Current and the Gulf of Lions (see boxes in Figure 1). For the Algerian Current, the reduction of the inverse cascade is mainly driven by the damping of the standing eddy near 6°E (not shown). In NOCRT, a too large a mesoscale activity leads to a too strong eddy-mean flow interaction. Noteworthy, over the Catalan Sea (see box in Figure 1), despite a similar EKE relative damping (by $\approx 25\%$) than the Algerian Current, the cascade of energy is only slightly reduced. This is explained by the absence of strong mean current and large mesoscale features such as the eddy near 6°E that has an important effect on the mean flow, which is largely mitigated by CFB. Note that as shown by Arbic et al. (2013) and Renault et al. (2019b), even for the World Ocean, the AVISO product does not allow to estimate properly the cascade of energy.

5.2. Alboran Gyres

As shown in Figures 2a and 2b, in the observations and in NOCRT, the Alboran Sea circulation is characterized by the presence of two anticyclonic gyres, namely the Western Alboran Gyre (WAG) and the Eastern Alboran Gyre (EAG). While the WAG has a year around persistence and is very well defined in the mean SSH field, the EAG, located between 2.5°W and 1.5°W, is less intense and mainly exists during summer (Renault et al., 2012b; Vargas-Yáñez et al., 2002; Á. Viúdez et al., 1996, 1998). It is therefore less defined than the WAG in both AVISO and NOCRT. The EAG is often poorly represented in oceanic models. It can be too weak as in Sannino et al. (2015) and NOCRT or too intense and persistent as e.g., in Juza et al. (2016) or e.g., Beuvier et al. (2012). As shown in the literature, the Alboran gyres are influenced by several factors such as the Atlantic Jet (AJ) that enters the Alboran Sea through the Strait of Gibraltar (e.g., García Lafuente et al. 2007; Parrilla & Kinder 1987; Tintoré et al. 1991; Á. Viúdez et al. 1996, 1998), but also the bathymetry of the Gibraltar strait (influencing also the Atlantic Jet), flow-topography interactions and the coastline (Sannino et al., 2015).

From NOCRT to CRT, both WAG and EAG mean intensities are reduced (Figure 2bc). CFB, by inducing large sinks of energy from mesoscale currents to the atmosphere (Figure 8a) acts as an eddy killer, reducing the mesoscale activity and, thus, the eddy-mean flow interactions (Figure 9a). The partial control of the EAG by CFB can also be revealed by estimating the Empirical Orthogonal Functions (EOFs) on the

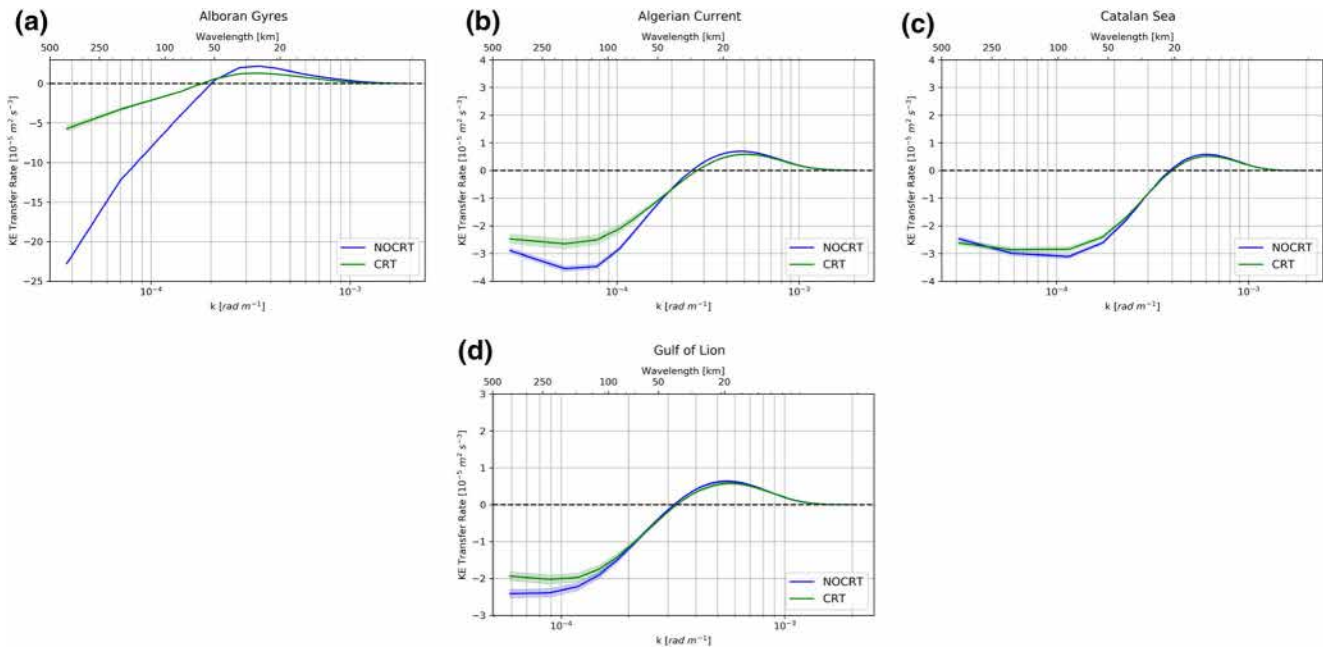


Figure 9. Spectral flux $\pi_{KE}(k)$ of surface oceanic geostrophic kinetic energy over the boxes represented in Figure 1 but excluding the lands for: (a) the Alboran Sea, (b) the Algerian Current, (c) for the Catalan Sea, and (d) the Gulf of Lions for coupled simulations without CFB (NOCRT, blue) and with CFB (CRT, red). The shaded curves represent the associated error as estimated using a bootstrap method. The CFB, via the *Eddy Killing* mitigates the inverse energy cascade, altering the Alboran Gyres and stabilizing the Algerian Current. CFB, current feedBack to the atmosphere.

SSH after removing the long-term mean state. The EOFs modes represent the variation of the circulation with respect to the mean state. Consistent with Renault et al. (2012b), the first EOF mode (not shown) explains $\approx 70\%$ of the variance and is a manifestation of the steric contribution of the seasonal signal, intensifying or weakening both WAG and EAG respectively during the spring–summer and the winter–fall. CFB does not have a significant impact on this mode. The second mode is depicted in Figures 10a and 10b and represents $\approx 13\%$ of the variance in both NOCRT and CRT. Its spatial pattern shows an intensification or a weakening of the EAG depending on the sign of the associated time series (Figure 10c). In CRT, the intensification (or weakening) of the EAG is less intense than that in NOCRT. As a result, the EAG is still formed but remains less intense than that in NOCRT because of CFB.

To sum up, CFB has a significant impact on the Alboran Gyres formation, intensities, and variabilities, and is therefore one more ingredient that should be taken into account when assessing the dynamics of the area.

5.3. Algerian Current and Transport of Particles from Gibraltar to Sardinia

The Algerian Current is an along slope current that flows along the North African coast. This current can meander and generates large anticyclonic eddies (diameter of at least 100 km, Millot & Taupier-Le-tage, 2005) that are reflected by a relatively large EKE (Figure 5). Strong and standing eddies near 6°E have been observed by Puillat et al. (2002); however, NOCRT is characterized by a classic bias, that is a too large a mesoscale activity with respect to the observations over that region (Figure 5) and the presence of too strong and frequent standing eddies that can be, as a result, seen in the mean SSH and mean associated circulation (Figures 2 and 3).

The net transport along the Algerian Current is estimated by following a Ψ contour of 0 Sv (as shown in Figure 3, this choice allows to effectively follow the Algerian Current) and by estimating the net transport as the difference between the maximal and minimal Ψ values across 100 km of the chosen contour (Figure 11, 150 km does not change the result). Consistent with Pacanowski (1987) and Luo et al. (2005), from NOCRT to CRT, the mean wind work ($F_m K_m$) is reduced by $\approx 15\%$ (not shown), which causes a slow-down of the

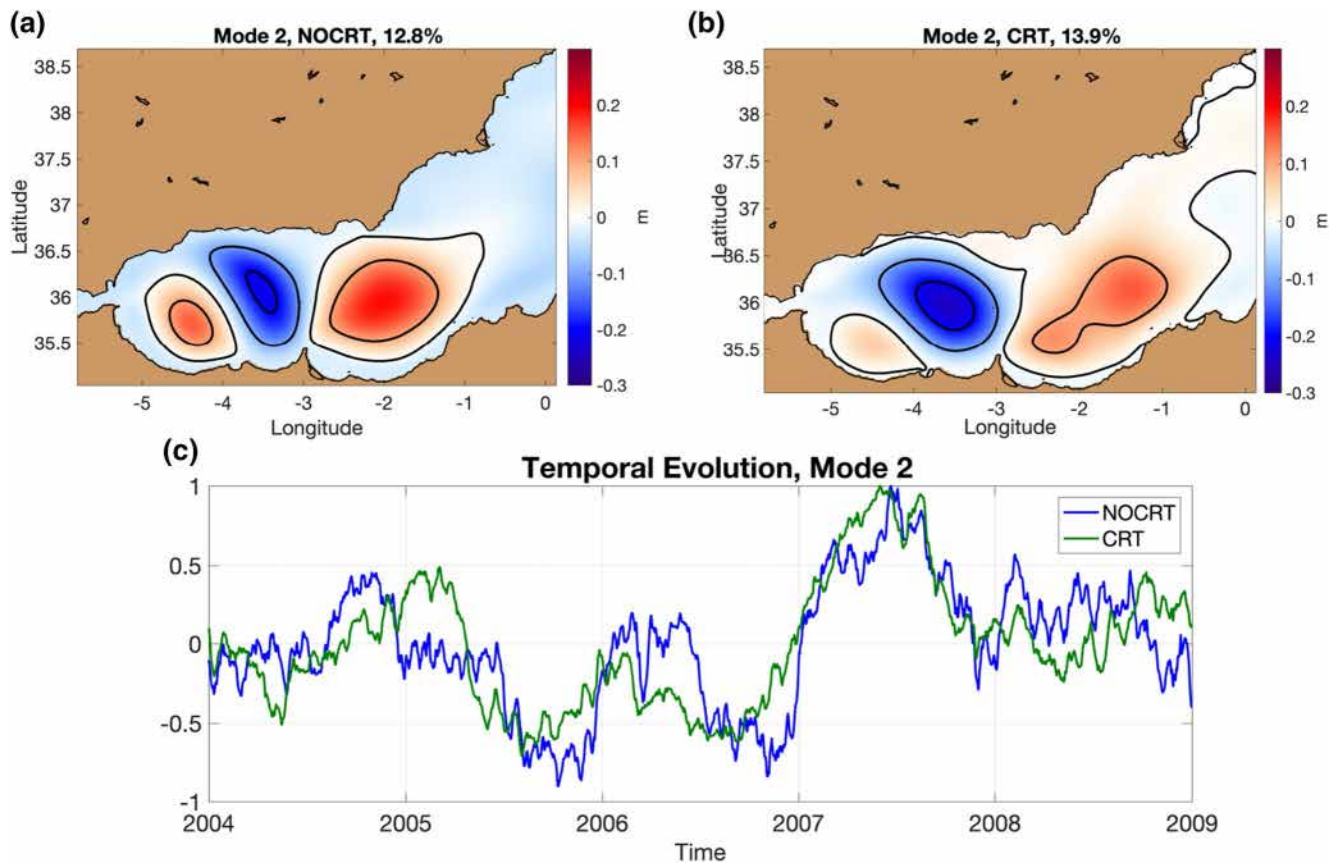


Figure 10. Spatial load and time evolution of the second mode of the Empirical Orthogonal Function (EOF) analysis of the SSH field. SSH, sea surface height.

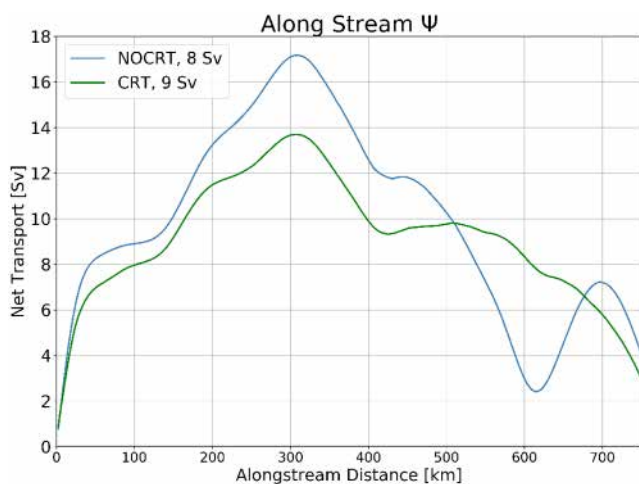


Figure 11. Ψ along the Algerian Current (see Figure 3), from NOCRT and CRT. On the one hand, CFB slows down the Algerian Current from NOCRT to CRT by 10% on average but up to 20%. On the other hand, in NOCRT, standing eddies near Sardinia causes a strong disruption of the Algerian Current, largely reducing the net transport. CFB, by damping these eddies, stabilizes this part of the Algerian Current. CFB, current feedBack to the atmosphere.

Algerian Current by $\approx 10\%$ on an average along its path but up to 20% when the Algerian Currents reaches its maximal values. In NOCRT, standing eddies near Sardinia causes a strong disruption of the Algerian Current, largely reducing the net transport from 12 Sv to 2.5 Sv. In contrast to NOCRT and as discussed in Section 4.1, CRT, through the *eddy killing* mechanism and the associated sinks of energy (Figure 8a), has a weaker and more realistic EKE along the Algerian Current near Sardinia than that in NOCRT. As a result, as demonstrated in Section 5.1, CFB causes a reduction of the inverse cascade of energy (Figure 9b), in particular near 6° E, and, thus, a stabilization of the Algerian Current that does not represent anymore the large drop of transport near 6° E.

From NOCRT to CRT, two mechanisms have an antagonistic effect on the Algerian Current and on its transport of water masses. On the one hand, the slow-down of the mean currents should delay particles. On the other hand, the damping of the mesoscale activity causes less meanders, which should reduce the traveling distance of the particles and, thus, make them travel faster. To assess the extent to which CFB alter the mean transport of particles through the alteration of the Alboran Gyres and of the Algerian Current, the trajectories of numerical Lagrangian floats are integrated using the ARIANE package (Blanke et al., 1999). Particles are seeded every day in the Gibraltar Strait (see blue line in Figure 1) over the whole water column (about 10^6 particles in total). The particles are advected using the daily mean velocity fields over a time span of 5-year

in NOCRT and CRT and intercepted in three sections highlighted by the bluish lines in Figure 1: the Ibiza channel, a section between Ibiza and Sardinia and a section between Sardinia and Africa. Two diagnostics are used: the arrival time of the particles that flow through the Ibiza and the Sardinia sections; and the corresponding density changes of the particles as a function of their arrival time.

Figure 12a depicts the probability density function (PDF) of the arrival time of the particles at the Ibiza Channel. About the same number of particles (~3%) flow through the Ibiza channel in NOCRT and CRT. However, as highlighted by the PDF and by the mean and median of the arrival time, from NOCRT to CRT, CFB causes a shift of the PDF to a longer arrival time, revealing a delay of the particles by ~10%. For these particles, the isopycnal mixing is not impacted by CFB (not shown). In NOCRT, 43% of the particles flow through the Sardinia section versus 50% in CRT (Figure 12b). This difference is explained by the presence of too strong and frequent standing eddies near 6° E in NOCRT. These eddies advect more particles northward, preventing them from reaching Sardinia. Additionally, as for the Ibiza section, CFB delay the particles, resulting in a shift of the PDF to a longer arrival time. From NOCRT to CRT, the mean and median travel times are increased by ~5% and ~11% respectively. Interestingly, particles reaching Sardinia are less mixed from NOCRT to CRT by 5%, which is likely due the less active mesoscale activity in CRT.

5.4. Retroflexion of the Northern Current and Transport through the Ibiza Channel

As shown in Figure 2a, in the observations, the Northern Current flows southwestward along the French and Catalan coasts and generally retroflects between the Ibiza Channel and ~40° N. Both simulations represent the Northern Current, however, they are both biased in their representation of its surface retroflexion, which is located too far downstream. In NOCRT (CRT), in winter, the inflow and outflow through the Ibiza Channel are 1.93 Sv and -1.38 Sv (1.86 Sv and -1.62 Sv) respectively, while in summer, the inflow and outflow are 1.92 Sv and -1.50 Sv (1.55 Sv and -1.28 Sv). Pinot et al. (2002) and Heslop et al. (2012) highlight from in situ observations the existence of a seasonal cycle of the net transport of 1 Sv, which is represented neither in NOCRT nor in CRT. Due to too much downstream retroflexion of the Northern Current, the outflow is too large in both simulations. It is interesting to note that, similar to the case of the North Atlantic basin (Renault et al., 2016b), from NOCRT to CRT, CFB induces a weakening of both inflow and outflow, which is probably due to the slow-down of the mean flow induced by the large-scale effect of CFB.

Although the mean retroflexion of the Northern Current is situated in the Catalan Sea, the Northern Current retroflexion can be classified in three categories: a classic retroflexion that roughly corresponds to the mean retroflexion position; an upstream retroflexion that is caused by the presence of large eddies, close to 41°N (Pascual et al., 2002); and a downstream retroflexion that can make the Northern Current cross the Ibiza channel. The position of the surface retroflexion of the Northern Current can be estimated using a method similar to that proposed by Loveday et al. (2014) for the Agulhas Current. The latitudinal position of the Northern Current is derived through a Sea Surface Height (SSH) contour and tracked through the 10-day averaged fields of the simulations and AVISO for the period 2004–2008. The value of the contour is determined from the SSH covering 43.6°N–43.8°N, 7.8°E–8.2°E and $h > 300$ m, i.e., a region where the flow is not too turbulent. The value of the southernmost contour is taken as the maximum extent of the loop (red point in Figure 13b). For each experiment and for AVISO, a meridional probability density function is computed by spatially grouping the estimated retroflexion positions into boxes of 1° latitude. Such a method successfully captures downstream retroflexion of the Northern Current (see e.g., Figure 13b) but has difficulties in capturing its upstream retroflexion (not shown). For this reason, we only use four boxes ranging from 37°N to 41°N. Figure 13a depicts the probability density function. In the observations, two categories of variability of the Northern current retroflexion can be defined. The first category represents a central retroflexion located north of 40°N. It represents 70% of the occurrences and also includes upstream retroflexion. The second category represents a downstream retroflexion and is illustrated in Figure 13b. Consistent with the previous results, from NOCRT to CRT, the distribution of the position of the retroflexion is approximately the same, indicating that CFB does not have a strong influence on the Northern Current surface downstream retroflexion. The distribution of the Northern Current retroflexion in Figure 13a also confirms the over-representation of down-

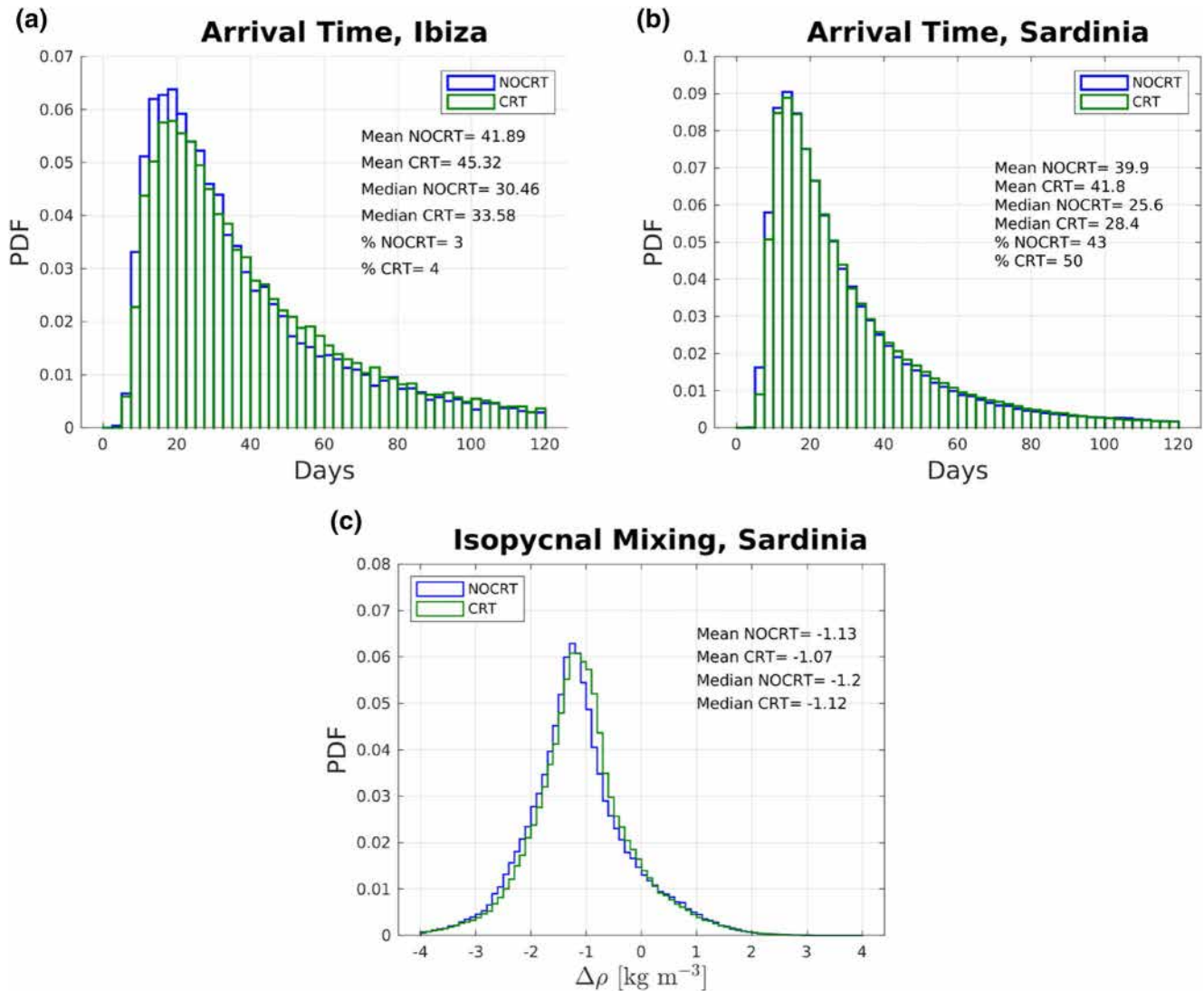


Figure 12. Arrival time of particles from the Gibraltar Strait to (a) the Ibiza Channel and (b) a section between Sardinia and Africa. (c) Density difference between the density of the particles at the Gibraltar Strait and that at Sardinia in function of the Arrival Time. The blue (green) color represents NOCRT (CRT).

stream retroflection in both simulations (about 70% vs. 30% in observations). The similar representation of the surface Northern Current in NOCRT and CRT can also be confirmed by applying an EOFs analysis on the SSH in the Catalan Sea. It shows that NOCRT and CRT have approximately the same modes of variability in the Catalan Sea (not shown). This is also consistent with Figure 9c that represents the energy cascade for the Catalan Sea, i.e., where the downstream retroflection of the Northern Current occurs. As shown in Section 5.1, despite a damping of the mesoscale activity in the Catalan Sea of about 25%, the inverse energy cascade, i.e., the eddy-mean flow interaction, in the Catalan Sea is only slightly affected by CFB.

Despite CFB does not strongly affect the surface retroflection of the Northern Current, Figure 3 reveals that CFB affects the barotropic transport by the Northern Current and the barotropic retroflection of the Northern Current. From a barotropic transport point of view, in NOCRT, the Northern Current retroflects upstream with respect to that in CRT, expressing more often an upstream retroflection. This is explained by a reduction of the inverse cascade of energy over the Gulf of Lions (Figures 9c and 9d) that mitigates short-cut of the mean barotropic current by eddies.

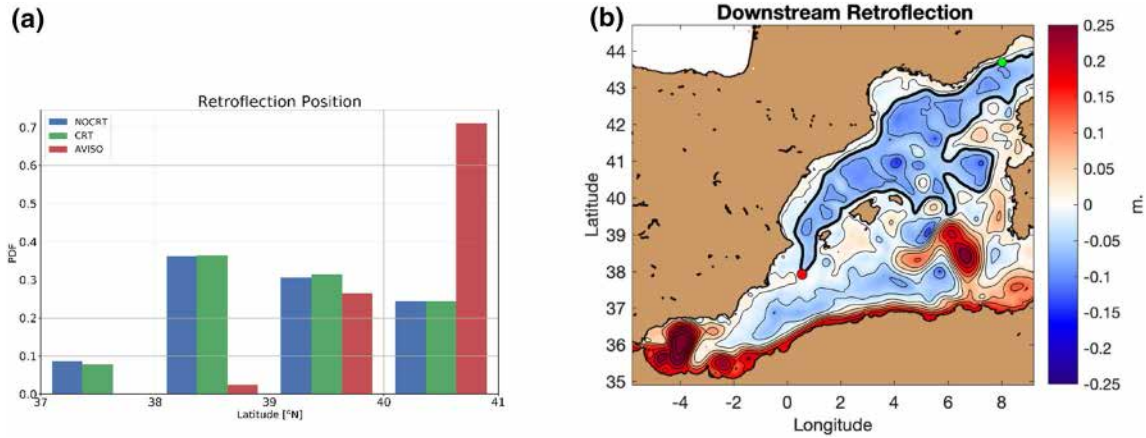


Figure 13. (a) Meridional distribution of the Northern current retroflection location for the period 2004–2008 from AVISO (red), NOCRT (blue), and CRT (green). Two categories of retroflection can be derived: a central retroflection and a downstream retroflection. CFB does not affect significantly the Northern Current retroflection. (b) Illustration of a downstream retroflection as estimated by the detection method (Section 5.4). The colors represent the sea surface height (SSH) from AVISO; the thick black contour represents the detected Northern current and the green and red dots the initial position of the detection and the Northern Current retroflection. CFB, current feedBack to the atmosphere. AVISO, Archiving, Validation and Interpretation of Satellite Oceanographic data.

6. Low-Level Wind and Surface Stress Response to Mesoscale Ocean-Atmosphere Coupling

6.1. Current Feedback Coupling Coefficients

As stated in Renault et al. (2019c), the CFB has a bottom-up effect, i.e., an upward effect. It first affects the surface stress, which in turn alters the low-level wind. CFB only has a systematic effect on the surface stress (wind) curl, but not on its divergence nor magnitude. To characterize, and then parameterize in a forced ocean model, the surface stress and wind responses to CFB, Renault et al. (2016c) and Renault et al. (2017a) define two coupling coefficients: s_τ , which is estimated as the slope between the mesoscale surface currents vorticity and surface stress curl; and s_w , which is the slope between the mesoscale surface current vorticity and wind curl (Section 2). As a first approximation, s_τ can be interpreted as a measure of the efficiency of the *eddy killing*: the more negative the s_τ , the more efficient the *eddy killing* is and, consequently, the larger the dampening of the mesoscale activity. The intensity of s_w indicates the efficiency of the partial re-energization of the ocean by the wind response to the CFB (Renault et al., 2016c, 2019c): the more positive the s_w , the more intense the partial re-energization of the ocean. In NOCRT, the two coupling coefficients are ≈ 0 (not shown) because the CFB is ignored. s_τ and s_w estimated from CRT are shown in Figure 14. Consistent with Renault et al. (2017a, 2019c), s_τ is characterized by a spatial variability (and a seasonal variability, not shown), and is negative everywhere, except where some orographic effects generate wind and subsequent wind-driven currents. s_τ has a domain-averaged value of $\overline{s_\tau} = -0.92 \cdot 10^{-2} \text{ N s m}^{-3}$. Consistent with previous studies, s_w is positive almost everywhere and has domain-averaged value of 0.21.

As suggested by Renault et al. (2016a, 2017a) and tested by Renault et al. (2020), in a forced ocean model, the wind response to the CFB can be estimated as:

$$U'_a = s_w U_o, \quad (10)$$

while the surface stress response can be approximated as:

$$\tau' = s_\tau U_o, \quad (11)$$

Renault et al. (2017a) demonstrate from satellite data that s_τ can be predicted from the large-scale wind as in the following:

$$s_\tau = \alpha |U_a| + \beta N \text{ m}^{-3} s, \quad (12)$$

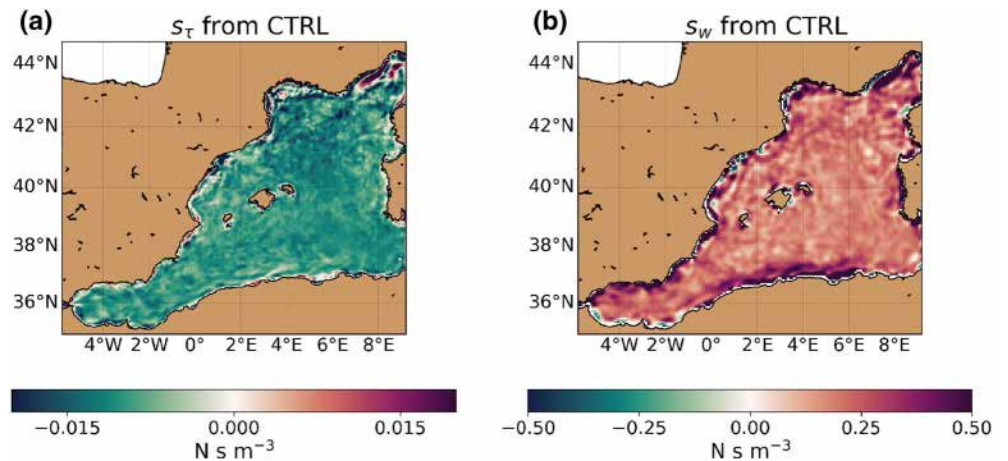


Figure 14. Coupling coefficients between (a) the mesoscale surface currents vorticity and the mesoscale surface stress curl (s_τ , see Section 2) and (b) the mesoscale surface currents vorticity and the mesoscale 10-m wind curl (s_w , see Section 2). Consistent with the literature, the CFB induces persistent surface stress curl anomalies that are anti-correlated with the surface currents. These anomalies are responsible of the sinks of energy in Figure 7. They also generate wind anomalies that are correlated with the surface currents and induce a partial re-energization of the ocean. CFB, current feedBack to the atmosphere.

Jullien et al. (2020) and Renault et al. (2020), using a quasi-global coupled model found values of $\alpha = 2.4 \cdot 10^{-3} \text{ N m}^{-4} \text{ s}^2$, and $\beta = 0.007 \text{ N m}^{-3} \text{ s}$. α and β are derived from the linear regression between the 10-m wind and s_τ and have an error bar of $\approx 20\%$. This relationship is verified for the Western Mediterranean region where the mean wind speed is $\approx 5.7 \text{ m s}^{-1}$, which corresponds to a predicted $\overline{s_\tau} = -0.86 \cdot 10^{-2} \text{ N s m}^{-3}$, i.e., close to the s_τ mean value ($\overline{s_\tau} = -0.92 \cdot 10^{-2} \text{ N s m}^{-3}$).

6.2. On the Thermal Feedback Coupling Coefficients

As for CFB, the TFB also induces mesoscale wind and stress curl anomalies that further generate additional Ekman pumping that can influence the propagation of eddies (Seo et al., 2016) and biogeochemical variability. As discussed in Section 2, Chelton et al. (2001) define four TFB coupling coefficients between the SST gradients and the curl (divergence) of wind and stress. As shown in Renault et al. (2019c), the coupling coefficient between mesoscale stress/wind curl and transverse stress/SST gradient (sC_w and sC_{str}) is contaminated by the effects of CFB. For this reason, all the TFB coupling coefficients are estimated from NOCRT. Figure 15 represents the four coefficients mentioned above. Consistent with the results obtained for other regions (e.g., Chelton et al., 2007; Desbiolles et al., 2014), the positivity of the coupling coefficients reflects the fact that mesoscale SST anomalies also induce 10 m wind and surface stress curl and divergence anomalies over the WMS. In some locations, the coefficients are negative and are probably contaminated by orographic effects (Renault et al., 2016a). Overall, the highest values of the curl coefficients (i.e., sC_w and sC_{str} , Figures 15a and 15c) highlight the regions where TFB induces the largest ocean vertical velocities.

7. Discussion

In this study, we have shown that current feedback to the atmosphere (CFB) plays an important role in determining WMS dynamics at both the large-scale and mesoscale. Similar to the case of the World Ocean, CFB has two main direct effects. First, it reduces the mean input of energy from the atmosphere into the ocean and subsequently slows down the mean circulation. On the other hand, the CFB acts like a mesoscale eddy killer by inducing energy sinks of energy from mesoscale oceanic currents into the atmosphere, thus, damping the mesoscale activity by about 25%. These two effects interact to a large extent and affect the WMS circulation and its intermittency, improving the realism of the simulation with respect to drift-

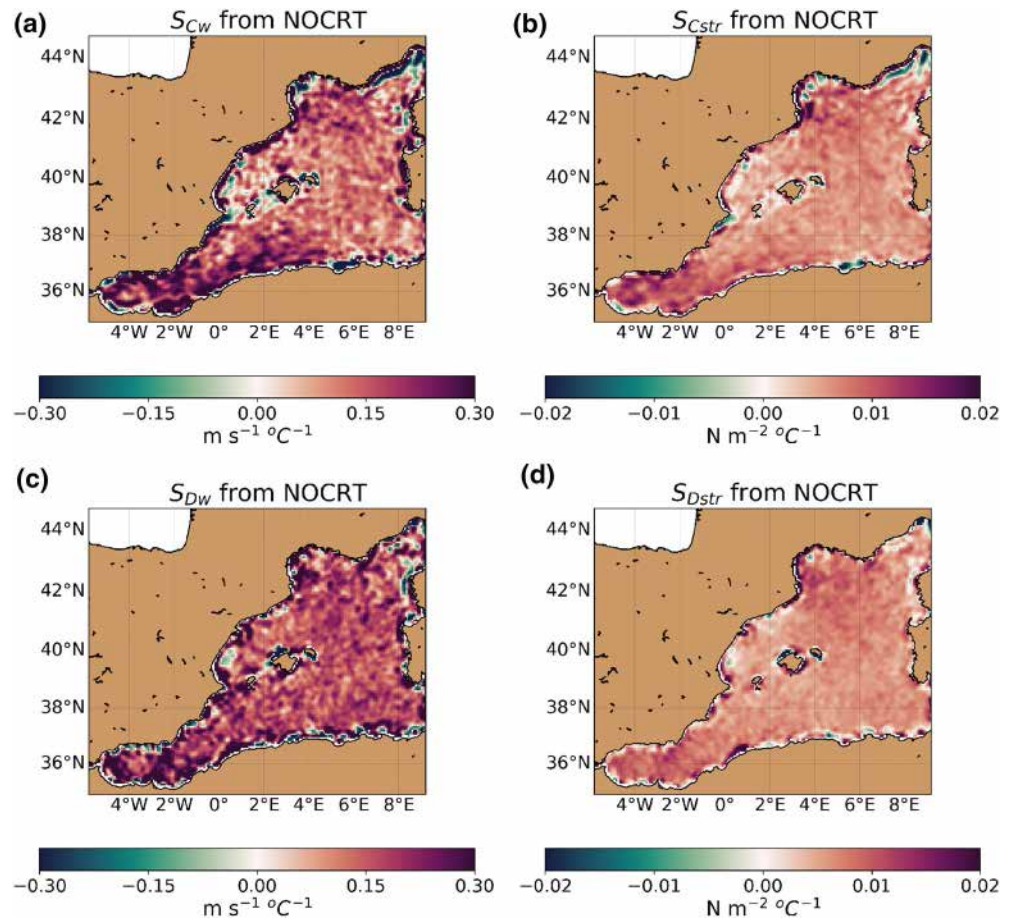


Figure 15. Thermal coupling coefficients (a) s_{Cw} , (b) s_{Cstr} , s_{Dw} , and s_{Dstr} as estimated from NOCRT (see Section 2). The TFB induces mesoscale wind (stress) curl and divergence anomalies, which are not correlated with the surface currents, and, thus, which do not induce conduits of energy between mesoscale oceanic currents and the atmosphere. TFB, thermal feedback.

ers observations. The effects of the CFB on the mean circulation are also revealed by a barotropic vorticity budget. We have shown that in the simulation that ignores CFB, the WMS cyclonic gyre circulation is mainly controlled by the curl of the surface stress and the nonlinear torque, which are compensated by the bottom drag and the bottom pressure torque. The CFB reduces wind stress curl and nonlinear torque effects by mitigating surface stress and slowing down the mean circulation and eddies. The bottom pressure torque becomes a second-order mechanism, revealing a flattening of the isopycnals by CFB. As for Western boundary currents, the reduction of the mesoscale activity weakens the eddy-mean flow interaction, altering Alboran Gyres and the Northern current retroflexion and stabilizing and slowing down the Algerian Current.

A simulation without CFB may overestimate the transport of water masses and biogeochemical materials by eddies. By weakening the strength of the Algerian Current and of its associated mesoscale activity, CFB also has a significant impact on the transport of particles, making them traveling slower and altering the associated isopycnal mixing. This has implications e.g., for connectivity studies and plastic Lagrangian advection studies. In the simulations analyzed in this study, the effect of the CFB rectifies long-standing biases of the Western Mediterranean Sea circulation that are present in eddy-rich oceanic models such as a too meandering an Algerian Current. It also alters emblematic features of the WMS such as the Alboran Gyres. However, CFB is obviously not the only driver of the WMS circulation. The Atlantic Jet, that flows through the Gibraltar strait, has a large control on the formation of the Alboran Gyres. Our simulations are, therefore, sensitive to the open boundary conditions and to the model used to force the simulations (MFS here). Other factors can also largely alter the Alboran Gyres, the Algerian Current, and the Northern Current such

as the vertical mixing parameterizations, but overall the bottom drag that plays an important role in the barotropic vorticity budget. However, our results confirm that the wind should not be considered only as a forcing that gives energy to the ocean initiating a turbulent cascade. It also has direct strong interactions at mesoscale and induces conduits of energy between the ocean and the atmosphere over the entire oceanic spectrum.

The CFB and TFB coupling coefficients have been estimated. Consistent with other regions of the World Ocean, the coupling coefficient between the mesoscale oceanic currents and surface stress curl (s_r) is negative everywhere and can be predicted from the large-scale wind or stress. Such a predicted coefficient can be used to mimic the CFB in a forced ocean model. Finally, the TFB coupling coefficients defined by Chelton et al. (2001) (sC_{str} , sD_{str} , sC_w , sD_w) have been estimated for the first time for the WMS. As for other regions, the SST mesoscale anomalies cause wind/stress curl and divergence anomalies. Both wind curl anomalies induced by the CFB and the TFB may be important to represent in a forced ocean model for the biogeochemistry as they cause additional oceanic vertical velocities by Ekman pumping. We intend to investigate this soon.

In summary, the effects of CFB highlighted in this study affect some of the main features of the dynamics in the WMS. Such an influence now needs to be assessed in climate simulations at basin scale, i.e., over the whole Mediterranean Sea and over a longer period of time. By altering the properties of the Atlantic water flowing from the Gibraltar Strait to Levantine basin, it is likely that CFB also affects the formation of the Levantine Intermediate Waters, and subsequently the deep water formation in the Aegean Sea, the Adriatic Sea, or in the Gulf of Lions. Also, as shown by Giordani et al. (2017), the deep water formation process itself over the Gulf of Lions is largely influenced by a strong mesoscale activity and important current-wind interactions during the deep-convection phase, hence, providing advantageous conditions for CFB. A similar methodology as in Waldman et al. (2017), i.e., based on ensemble simulations to discriminate the chaotic nature of the ocean, must be performed to confirm this hypothesis and understand the extent to which the CFB can influence deep water formation over the Gulf of Lions (or other deep water convection sites). From an atmospheric point of view, as for the Agulhas Current (Renault et al., 2017b), in addition to the induced mesoscale wind anomaly, the CFB might have a large influence on precipitation by changing the mean oceanic circulation and the near-surface water masses. A regional high-resolution atmospheric model is usually very expensive compared to a forced oceanic model. To estimate the oceanic response to CFB on a basin and climate scale, the CFB parameterizations proposed by Renault et al. (2020) could, therefore, be used within the framework of a forced oceanic model.

Data Availability Statement

Data can be downloaded from <http://research.atmos.ucla.edu/lrenault/WMED/>

Acknowledgments

The authors appreciate support from the National Science Foundation (OCE-1419450). This work used the GENCI #A0050107298 computing resources and the Engineering Discovery Environment (XSEDE, #TG-OCE150004). L. Renault and T. Arsouze would like to thank HPC-Europa3 program, application HPC17IUTPN and HPC17MM0RX, respectively, and Barcelona Supercomputing Center (BSC) for hosting them. L. Renault would like to thank the Institut de Ciències del Mar in Barcelona for hosting him. The authors thank J. Isern-Fontanet for useful discussions.

References

- Alberola, C., Millot, C., & Font, J. (1995). On the seasonal and mesoscale variabilities of the Northern Current during the PRIMO-0 experiment in the western Mediterranean-sea. *Oceanologica Acta*, 18(2), 163–192.
- Amores, A., Jordà, G., Arsouze, T., & Le Sommer, J. (2018). Up to what extent can we characterize ocean eddies using present-day gridded altimetric products?. *Journal of Geophysical Research: Oceans*, 123(10), 7220–7236.
- Arbic, B. K., Polzin, K. L., Scott, R. B., Richman, J. G., & Shriver, J. F. (2013). On eddy viscosity, energy cascades, and the horizontal resolution of gridded satellite altimeter products. *Journal of Physical Oceanography*, 43(2), 283–300.
- Beranger, K., Drillet, Y., Houssais, M.-N., Testor, P., Bourdalle-Badie, R., Alhammoud, B., et al. (2010). Impact of the spatial distribution of the atmospheric forcing on water mass formation in the Mediterranean Sea. *Journal of Geophysical Research*, 115(C12).
- Berthou, S., Mailler, S., Drobinski, P., Arsouze, T., Bastin, S., Béranger, K., & Brossier, C. L. (2018). Lagged effects of the Mistral wind on heavy precipitation through ocean-atmosphere coupling in the region of Valencia (Spain). *Climate Dynamics*, 51(3), 969–983.
- Berthou, S., Mailler, S., Drobinski, P., Arsouze, T., Bastin, S., Béranger, K., et al. (2016). Influence of submonthly air-sea coupling on heavy precipitation events in the Western Mediterranean basin. *Quarterly Journal of the Royal Meteorological Society*, 142, 453–471.
- Beuvier, J., Béranger, K., Lebeaupin Brossier, C., Somot, S., Sevault, F., Drillet, Y., et al. (2012). Spreading of the Western Mediterranean Deep Water after winter 2005: Time scales and deep cyclone transport. *Journal of Geophysical Research*, 117(C7).
- Blanke, B., Arhan, M., Madec, G., & Roche, S. (1999). Warm water paths in the equatorial Atlantic as diagnosed with a general circulation model. *Journal of Physical Oceanography*, 29(11), 2753–2768.
- Bouffard, J., Renault, L., Ruiz, S., Pascual, A., Dufau, C., & Tintoré, J. (2012). Sub-surface small-scale eddy dynamics from multi-sensor observations and modeling. *Progress in Oceanography*, 106, 62–79.
- Bye, J. A. (1985). Large-scale momentum exchange in the coupled atmosphere-ocean. *Elsevier Oceanography Series*, 40, 5161.

- Capet, X., McWilliams, J., Molemaker, M., & Shchepetkin, A. (2008). Mesoscale to submesoscale transition in the California Current System. Part I: Flow structure, eddy flux, and observational tests. *Journal of Physical Oceanography*, 38, 29–43.
- Chelton, D. B., DeSzoeke, R. A., Schlax, M. G., El Naggar, K., & Siwertz, N. (1998). Geographical variability of the first baroclinic Rossby radius of deformation. *Journal of Physical Oceanography*, 28(3), 433–460.
- Chelton, D. B., Esbensen, S. K., Schlax, M. G., Thum, N., Freilich, M. H., Wentz, F. J., et al. (2001). Observations of coupling between surface wind stress and sea surface temperature in the eastern tropical Pacific. *Journal of Climate*, 14(7), 1479–1498.
- Chelton, D. B., Schlax, M. G., Freilich, M. H., & Milliff, R. F. (2004). Satellite measurements reveal persistent small-scale features in ocean winds. *Science*, 303(5660), 978–983.
- Chelton, D. B., Schlax, M. G., & Samelson, R. M. (2007). Summertime coupling between sea surface temperature and wind stress in the California Current System. *Journal of Physical Oceanography*, 37(3), 495–517.
- Chelton, D. B., Schlax, M. G., & Samelson, R. M. (2011). Global observations of nonlinear mesoscale eddies. *Progress in Oceanography*, 51(2), 167–216.
- Chelton, D. B., & Xie, S.-P. (2010). Coupled ocean-atmosphere interaction at oceanic mesoscales. *Oceanography*, 23(4), 52–69.
- Dai, A., & Trenberth, K. E. (2002). Estimates of freshwater discharge from continents: Latitudinal and seasonal variations. *Journal of Hydrometeorology*, 3(6), 660–687.
- de la Vara, A., del Sastre, P. G., Arsouze, T., Gallardo, C., & Gaertner, M. Á. (2019). Role of atmospheric resolution in the long-term seasonal variability of the Tyrrhenian Sea circulation from a set of ocean hindcast simulations 1997–2008. *Ocean Modelling*, 134, 51–67.
- Debreu, L., Marchesiello, P., Penven, P., & Cambon, G. (2012). Two-way nesting in split-explicit ocean models: Algorithms, implementation and validation. *Ocean Modelling*, 49, 1–21.
- Desbiolles, F., Blanke, B., Bentamy, A., & Grima, N. (2014). Origin of fine-scale wind stress curl structures in the Benguela and Canary upwelling systems. *Journal of Geophysical Research: Oceans*, 119(11), 7931–7948.
- Dewar, W. K., & Flierl, G. R. (1987). Some effects of the wind on rings. *Journal of Physical Oceanography*, 17(10), 1653–1667.
- Duhaut, T. H., & Straub, D. N. (2006). Wind stress dependence on ocean surface velocity: Implications for mechanical energy input to ocean circulation. *Journal of Physical Oceanography*, 36(2), 202–211.
- Escudier, R., Renault, L., Pascual, A., Brasseur, P., Chelton, D., & Beuvier, J. (2016). Eddy properties in the Western Mediterranean Sea from satellite altimetry and a numerical simulation. *Journal of Geophysical Research: Oceans*, 121(6), 3990–4006.
- Estournel, C., Durrieu de Madron, X., Marsaleix, P., Auclair, F., Jullian, C., & Vehil, R. (2003). Observation and modeling of the winter coastal oceanic circulation in the Gulf of Lion under wind conditions influenced by the continental orography (FETCH experiment). *Journal of Geophysical Research*, 108(C3).
- Fairall, C., Bradley, E. F., Hare, J., Grachev, A., & Edson, J. (2003). Bulk parameterization of air-sea fluxes: Updates and verification for the COARE algorithm. *Journal of Climate*, 16(4), 571–591.
- Flamant, C. (2003). Alpine lee cyclogenesis influence on air-sea heat exchanges and marine atmospheric boundary layer thermodynamics over the western Mediterranean during a Tramontane/Mistral event. *Journal of Geophysical Research*, 108(C2).
- Freedman, D., & Diaconis, P. (1981). On the histogram as a density estimator: L 2 theory. *Zeitschrift für Wahrscheinlichkeitstheorie und Verwandte Gebiete*, 57(4), 453–476.
- García Lafuente, J., Sánchez Román, A., Díaz del Río, G., Sannino, G., & Sánchez Garrido, J. (2007). Recent observations of seasonal variability of the Mediterranean outflow in the Strait of Gibraltar. *Journal of Geophysical Research*, 112(C10).
- Gaube, P., Chelton, D. B., Samelson, R. M., Schlax, M. G., & O'Neill, L. W. (2015). Satellite observations of mesoscale eddy-induced Ekman pumping. *Journal of Physical Oceanography*, 45(1), 104–132.
- Giordani, H., Lebeaupin-Brossier, C., Leger, F., & Caniaux, G. (2017). A PV-approach for dense water formation along fronts: Application to the Northwestern Mediterranean. *Journal of Geophysical Research: Oceans*, 122(2), 995–1015. <https://doi.org/10.1002/2016JC012019>
- Guihou, K., Marmain, J., Ourmieres, Y., Molcard, A., Zakardjian, B., & Forget, P. (2013). A case study of the mesoscale dynamics in the North-Western Mediterranean Sea: a combined data-model approach. *Ocean Dynamics*, 63(7), 793–808.
- Hamon, M., Beuvier, J., Somot, S., Lellouche, J.-M., Greiner, E., Jordà, G., et al. (2016). Design and validation of MEDRYS, a Mediterranean Sea reanalysis over the period 1992–2013. *Ocean Science*, 12(2), 577–599. <https://doi.org/10.5194/os-12-577-2016>
- Heslop, E. E., Ruiz, S., Allen, J., López-Jurado, J. L., Renault, L., & Tintoré, J. (2012). Autonomous underwater gliders monitoring variability at “choke points” in our ocean system: A case study in the Western Mediterranean Sea. *Geophysical Research Letters*, 39(20).
- Isern-Fontanet, J., García-Ladona, E., & Font, J. (2003). Identification of Marine Eddies from Altimetric Maps. *Journal of Atmospheric and Oceanic Technology*, 20(5), 772–778.
- Isern-Fontanet, J., García-Ladona, E., & Font, J. (2006). Vortices of the Mediterranean Sea: An altimetric perspective. *Journal of Physical Oceanography*, 36(1), 87–103.
- Jackson, L., Hughes, C. W., & Williams, R. G. (2006). Topographic control of basin and channel flows: The role of bottom pressure torques and friction. *Journal of Physical Oceanography*, 36(9), 1786–1805.
- Jansá, A. (1987). Distribution of the mistral: A satellite observation. *Meteorology and Atmospheric Physics*, 36(1), 201–214.
- Jullien, S., Masson, S., Oerder, V., Samson, G., Colas, F., & Renault, L. (2020). Impact of ocean-atmosphere current feedback on the ocean mesoscale activity: regional variations, and sensitivity to model resolution. *Journal of Climate*, 33(7), 2585–2602.
- Juza, M., Mourre, B., Renault, L., Gómara, S., Sebastián, K., Lora, S., et al. (2016). SOCIB operational ocean forecasting system and multi-platform validation in the Western Mediterranean Sea. *Journal of Operational Oceanography*, 9(Suppl1), s155–s166.
- Karimova, S. (2019). Basin- to mesoscale surface circulation of the Western Mediterranean manifested by satellite-derived data products. *Remote Sensing of Environment*, 222, 50–64. <https://doi.org/10.1016/j.rse.2018.12.004>
- LaCasce, J. (2012). Surface quasigeostrophic solutions and baroclinic modes with exponential stratification. *Journal of Physical Oceanography*, 42(4), 569–580.
- Large, W. G., McWilliams, J. C., & Doney, S. C. (1994). Oceanic vertical mixing: A review and a model with a nonlocal boundary layer parameterization. *Reviews of Geophysics*, 32(4), 363–404.
- Le Corre, M., Gula, J., & Tréguier, A.-M. (2020). Barotropic vorticity balance of the north atlantic subpolar gyre in an eddy-resolving model. *Ocean Science*, 16(2), 451–468.
- Lebeaupin Brossier, C., & Drobinski, P. (2009). Numerical high-resolution air-sea coupling over the Gulf of Lions during two tramontane/mistral events. *Journal of Geophysical Research: Atmosphere*, 114(D10).
- Lemarié, F. (2015). Numerical modification of atmospheric models to include the feedback of oceanic currents on air-sea fluxes in ocean-atmosphere coupled models, Technical Report RT-464, INRIA Grenoble – Rhône-Alpes; Laboratoire Jean Kuntzmann; Université de Grenoble I – Joseph Fourier. INRIA.

- Loveday, B. R., Durgadoo, J. V., Reason, C. J., Biastoch, A., & Penven, P. (2014). Decoupling of the Agulhas leakage from the Agulhas Current. *Journal of Physical Oceanography*, 44(7), 1776–1797.
- Luo, J.-J., Masson, S., Roeckner, E., Madec, G., & Yamagata, T. (2005). Reducing climatology bias in an ocean-atmosphere CGCM with improved coupling physics. *Journal of Climate*, 18(13), 2344–2360.
- Mancho, A. M., Hernandez-Garcia, E., Small, D., Wiggins, S., & Fernandez, V. (2008). Lagrangian transport through an ocean front in the Northwestern Mediterranean Sea. *Journal of Physical Oceanography*, 38(6), 1222–1237.
- Marchesiello, P., Capet, X., Menkes, C., & Kennan, S. C. (2011). Submesoscale dynamics in tropical instability waves. *Ocean Modelling*, 39(1), 31–46.
- Marchesiello, P., McWilliams, J. C., & Shchepetkin, A. (2003). Equilibrium structure and dynamics of the California Current System. *Journal of Physical Oceanography*, 33(4), 753–783.
- Meroni, A. N., Renault, L., Parodi, A., & Pasquero, C. (2018). Role of the oceanic vertical thermal structure in the modulation of heavy precipitations over the Ligurian Sea. In *Meteorology and Climatology of the Mediterranean and Black Seas*. (pp. 391–410). Birkhäuser, Cham.
- Millot, C. (1979). Wind induced upwellings in the Gulf of Lions. *Oceanologica Acta*, 2, 261–274.
- Millot, C., & Taupier-Letage, I. (2005). Circulation in the Mediterranean sea. *The Mediterranean Sea* (pp. 29–66). New York: Springer.
- Mkhinini, N., Coimbra, A. L. S., Stegner, A., Arsouze, T., Taupier-Letage, I., & Béranger, K. (2014). Long-lived mesoscale eddies in the eastern Mediterranean Sea: Analysis of 20 years of AVISO geostrophic velocities. *Journal of Geophysical Research: Oceans*, 119(12), 8603–8626.
- Nakanishi, M., & Niino, H. (2006). An improved Mellor–Yamada level-3 model: Its numerical stability and application to a regional prediction of advection fog. *Boundary-Layer Meteorology*, 119(2), 397–407.
- O'Neill, L. W., Chelton, D. B., & Esbensen, S. K. (2010). The effects of SST-induced surface wind speed and direction gradients on midlatitude surface vorticity and divergence. *Journal of Climate*, 23(2), 255–281.
- Oerder, V., Colas, F., Echevin, V., Masson, S., & Lemarié, F. (2018). Impacts of the mesoscale ocean-atmosphere coupling on the Peru-Chile ocean dynamics: The current-induced wind stress modulation. *Journal of Geophysical Research: Oceans*, 123(2), 812–833.
- O'Neill, L. W., Chelton, D. B., & Esbensen, S. K. (2012). Covariability of surface wind and stress responses to sea surface temperature fronts. *Journal of Climate*, 25(17), 5916–5942.
- Pacanowski, R. (1987). Effect of equatorial currents on surface stress. *Journal of Physical Oceanography*, 17(6), 833–838.
- Parrilla, G., & Kinder, T. H. (1987). *The physical oceanography of the Alboran Sea* (Technical Rep.). NAVAL OCEAN RESEARCH AND DEVELOPMENT ACTIVITY NSTL STATION MS.
- Pascual, A., Buongiorno Nardelli, B., Larnicol, G., Emelianov, M., & Gomis, D. (2002). A case of an intense anticyclonic eddy in the Balearic Sea (western Mediterranean). *Journal of Geophysical Research*, 107(C11), 4–1.
- Pinot, J.-M., López-Jurado, J. L., & Riera, M. (2002). The CANALES experiment (1996–1998). Interannual, seasonal, and mesoscale variability of the circulation in the Balearic Channels. *Progress in Oceanography*, 55(3–4), 335–370.
- Poulain, P.-M., Menna, M., & Mauri, E. (2012). Surface geostrophic circulation of the Mediterranean Sea derived from drifter and satellite altimeter data. *Journal of Physical Oceanography*, 42(6), 973–990.
- Puillat, I., Taupier-Letage, I., & Millot, C. (2002). Algerian Eddies lifetime can near 3 years. *Journal of Marine Systems*, 31(4), 245–259. [https://doi.org/10.1016/S0924-7963\(01\)00056-2](https://doi.org/10.1016/S0924-7963(01)00056-2)
- Renault, L., Chiggiato, J., Warner, J. C., Gomez, M., Vizoso, G., & Tintore, J. (2012a). Coupled Atmosphere-Ocean-Wave simulations of a storm event over the Gulf of Lion and Balearic Sea. *Journal of Geophysical Research*, 117(C9).
- Renault, L., Hall, A., & McWilliams, J. C. (2016a). Orographic Shaping of U.S. West Coast Wind Profiles During the Upwelling Season. *Climate Dynamics*, 1–17.
- Renault, L., Lemarié, F., & Arsouze, T. (2019a). On the implementation and consequences of the oceanic currents feedback in ocean-atmosphere coupled models. *Ocean Modelling*, 141(101), 423.
- Renault, L., Marchesiello, P., Masson, S., & McWilliams, J. C. (2019b). Remarkable control of western boundary currents by eddy killing, a mechanical air-sea coupling process. *Geophysical Research Letters*, 46(5), 2743–2751.
- Renault, L., Masson, S., Arsouze, T., Madec, G., & McWilliams, J. C. (2020). Recipes for how to force oceanic model dynamics. *Journal of Advances in Modeling Earth Systems*, 12(2), 715, e2019MS001.
- Renault, L., Masson, S., Oerder, V., Jullien, S., & Colas, F. (2019c). Disentangling the mesoscale ocean-atmosphere interactions. *Journal of Geophysical Research: Oceans*, 124(3), 2164–2178.
- Renault, L., McWilliams, J. C., & Gula, J. (2018). Dampening of submesoscale currents by air-sea stress coupling in the californian upwelling system. *Scientific Reports*, 8(1), 388.13
- Renault, L., McWilliams, J. C., & Masson, S. (2017a). Satellite observations of imprint of oceanic current on wind stress by air-sea coupling. *Scientific Reports*, 7(1), 747.17
- Renault, L., McWilliams, J. C., & Penven, P. (2017b). Modulation of the agulhas current retroflection and leakage by oceanic current interaction with the atmosphere in coupled simulations. *Journal of Physical Oceanography*, 47(8), 2077–2100.
- Renault, L., Molemaker, M. J., Gula, J., Masson, S., & McWilliams, J. C. (2016b). Control and Stabilization of the Gulf Stream by oceanic current interaction with the atmosphere. *Journal of Physical Oceanography*, 46(11), 3439–3453.
- Renault, L., Molemaker, M. J., McWilliams, J. C., Shchepetkin, A. F., Lemarié, F., Chelton, D., et al. (2016c). Modulation of wind work by oceanic current interaction with the atmosphere. *Journal of Physical Oceanography*, 46(6), 1685–1704.
- Renault, L., Oguz, T., Pascual, A., Vizoso, G., & Tintore, J. (2012b). Surface circulation in the Alborán Sea (western Mediterranean) inferred from remotely sensed data. *Journal of Geophysical Research*, 117(C8).
- Ridgway, K., Dunn, J., & Wilkin, J. (2002). Ocean interpolation by four-dimensional weighted least squares: Application to the waters around Australasia. *Journal of Atmospheric and Oceanic Technology*, 19(9), 1357–1375.
- Rio, M.-H., Mulet, S., & Picot, N. (2014). Beyond GOCE for the ocean circulation estimate: Synergetic use of altimetry, gravimetry, and in situ data provides new insight into geostrophic and Ekman currents. *Geophysical Research Letters*, 41(24), 8918–8925.
- Ruiz, S., Renault, L., Garau, B., & Tintore, J. (2012). Underwater glider observations and modeling of an abrupt mixing event in the upper ocean. *Geophysical Research Letters*, 39(1).
- Saha, S., Moorthi, S., Pan, H.-L., Wu, X., Wang, J., Nadiga, S., et al. (2010). The NCEP climate forecast system reanalysis. *Bulletin of the American Meteorological Society*, 91(8), 1015–1057.
- Sandwell, D. T., & Smith, W. H. (1997). Marine gravity anomaly from Geosat and ERS 1 satellite altimetry. *Journal of Geophysical Research*, 102(B5), 10039–10054 1978–2012.

- Sannino, G., Carillo, A., Pisacane, G., & Naranjo, C. (2015). Mesoscale surface circulation of the in modelling the Mediterranean thermohaline circulation. *Progress in Oceanography*, 134, 304–329. <https://doi.org/10.1016/j.pocean.2015.03.002>
- Sayol, J.-M., Orfila, A., Simarro, G., López, C., Renault, L., Galán, A., & Conti, D. (2013). Sea surface transport in the Western Mediterranean Sea: a Lagrangian perspective. *Journal of Geophysical Research: Oceans*, 118(12), 6371–6384.
- Schoonover, J., Dewar, W., Wienders, N., Gula, J., McWilliams, J. C., Molemaker, M. J., et al. (2016). North Atlantic barotropic vorticity balances in numerical models. *Journal of Physical Oceanography*, 46(1), 289–303.
- Scott, R. B., & Xu, Y. (2009). An update on the wind power input to the surface geostrophic flow of the World Ocean. *Deep Sea Research I: Oceanographic Research Papers*, 56(3), 295–304.
- Seo, H. (2017). Distinct influence of air–sea interactions mediated by mesoscale sea surface temperature and surface current in the Arabian Sea. *Journal of Climate*, 30(20), 8061–8080.
- Seo, H., Miller, A. J., & Norris, J. R. (2016). Eddy–wind interaction in the California Current System: Dynamics and impacts. *Journal of Physical Oceanography*, 46(2), 439–459.
- Shchepetkin, A. F. (2015). An adaptive, Courant-number-dependent implicit scheme for vertical advection in oceanic modeling. *Ocean Modelling*, 91, 38–69.
- Shchepetkin, A. F., & McWilliams, J. C. (2005). The Regional Oceanic Modeling System (ROMS): A split-explicit, free-surface, topography-following-coordinate oceanic model. *Ocean Modelling*, 9(4), 347–404.
- Shchepetkin, A. F., & McWilliams, J. C. (2009). Correction and commentary for “Ocean forecasting in terrain-following coordinates: Formulation and skill assessment of the regional ocean modeling system” by Haidvogel et al., J. Comp. Phys. 227. 3595–3624. *Journal of Computational Physics*, 228(24), 8985–9000.
- Skamarock, W., Klemp, J., Dudhia, J., Gill, D., & Barker, D. (2008). *A description of the Advanced Research WRF version 3*. NCAR (Technical Report). Note NCAR/TN-4751STR.
- Small, R., Xie, S., O'Neill, L., Seo, H., Song, Q., Cornillon, P., et al. (2008). Air–sea interaction over ocean fronts and eddies. *Dynamics of Atmospheres and Oceans*, 45, 274–319.
- Somot, S., Houpert, L., Sevault, F., Testor, P., Bosse, A., Taupier-Letage, I., et al. (2018). Characterizing, modelling and understanding the climate variability of the deep water formation in the North-Western Mediterranean Sea. *Climate Dynamics*, 51(3), 1179–1210.
- Takatama, K., & Schneider, N. (2017). The Role of Back Pressure in the Atmospheric Response to Surface Stress Induced by the Kuroshio. *Journal of the Atmospheric Sciences*, 74(2), 597–615.
- Testor, P., Bosse, A., Houpert, L., Margirier, F., Mortier, L., Legoff, H., & Conan, P., et al. (2018). Multiscale observations of deep convection in the northwestern Mediterranean Sea during winter 2012–2013 using multiple platforms. *Journal of Geophysical Research: Oceans*, 123(3), 1745–1776. <https://doi.org/10.1002/2016JC012671>
- Tintoré, J., Gomis, D., Alonso, S., & Parrilla, G. (1991). Mesoscale dynamics and vertical motion in the Alboran Sea. *Journal of Physical Oceanography*, 21(6), 811–823.
- Tonani, M., Teruzzi, A., Korres, G., Pinardi, N., Crise, A., Adani, M., et al. (2011). The Mediterranean Monitoring and Forecasting Centre, a component of the MyOcean system. *Proceedings of the sixth international conference on EuroGOOS* (pp. 4–6).
- Valcke, S. (2013). The OASIS3 coupler: A European climate modelling community software. *Geoscientific Model Development*, 6(2), 373–388.
- Vargas-Yáñez, M., Plaza, F., Garcia-Lafuente, J., Sarhan, T., Vargas, J., & Vélez-Belchí, P. (2002). About the seasonal variability of the Alboran Sea circulation. *Journal of Marine Systems*, 35(3–4), 229–248.
- Viúdez, Á., Tintoré, J., & Haney, R. L. (1996). Circulation in the Alboran Sea as determined by quasi-synoptic hydrographic observations. Part I: Three-dimensional structure of the two anticyclonic gyres. *Journal of Physical Oceanography*, 26(5), 684–705.
- Viúdez, A., Pinot, J.-M., & Haney, R. (1998). On the upper layer circulation in the Alboran Sea. *Journal of Geophysical Research*, 103(C10), 21653–21666.
- Waldman, R., Somot, S., Herrmann, M., Bosse, A., Caniaux, G., Estournel, C., et al. (2017). Modeling the intense 2012–2013 dense water formation event in the northwestern Mediterranean Sea: Evaluation with an ensemble simulation approach. *Journal of Geophysical Research: Oceans*, 122(2), 1297–1324.
- Winant, C., Dorman, C., Friehe, C., & Beardsley, R. (1988). The marine layer off northern California: An example of supercritical channel flow. *Journal of the Atmospheric Sciences*, 45(23), 3588–3605.
- Xu, Y., & Scott, R. B. (2008). Subtleties in forcing eddy resolving ocean models with satellite wind data. *Ocean Modelling*, 20(3), 240–251.